A&A 675, A150 (2023)
https://doi.org/10.1051/0004-6361/202245749

Astronomy & Astrophysics

Effects of multiphase gas and projection on X-ray observables in simulated galaxy clusters as seen by eROSITA

J. ZuHone[1], Y. E. Bahar[2], V. Biffi[3,4], K. Dolag[5,6], J. Sanders[2], E. Bulbul[2], T. Liu[2], T. Dauser[7], O. König[7], X. Zhang[2], and V. Ghirardini[2]

[1] Center for Astrophysics, Harvard and Smithsonian, 60 Garden St., Cambridge, MA 02138, USA
e-mail: john.zuhone@cfa.harvard.edu
[2] Max-Planck-Institut für Extraterrestrische Physik (MPE), Gießenbachstraße 1, 85748 Garching bei München, Germany
[3] INAF – Osservatorio Astronomico di Trieste, Via Tiepolo 11, 34143 Trieste, Italy
[4] IFPU – Institute for Fundamental Physics of the Universe, Via Beirut 2, 34014 Trieste, Italy
[5] Universitäts-Sternwarte, Fakultät für Physik, Ludwig-Maximilians-Universität München, Scheinerstr. 1, 81679 München, Germany
[6] Max-Planck-Institut für Astrophysik (MPA), Karl-Schwarzschild-Straße 1, 85748 Garching bei München, Germany
[7] Remeis-Observatory & ECAP, FAU Erlangen-Nürnberg, Sternwartstr. 7, 96049 Bamberg, Germany

Received 21 December 2022 / Accepted 10 May 2023

ABSTRACT

Context. Galaxy clusters are the most massive bound objects in the recent history of the universe; the number density of galaxy clusters as a function of mass and redshift is a sensitive function of the cosmological parameters. To use clusters for cosmological parameter studies, it is necessary to determine their masses as accurately as possible, which is typically done via scaling relations between mass and observables.

Aims. X-ray observables can be biased by a number of effects, including multiphase gas and projection effects, especially in the case where cluster temperatures and luminosities are estimated from single-model fits to all of the emission with an overdensity radius such as r_{500c}. Using simulated galaxy clusters from a realistic cosmological simulation, our aim is to determine the importance of these biases in the context of Spectrum-Roentgen-Gamma/eROSITA observations of clusters.

Methods. We extracted clusters from the `Box2_hr` simulation from the Magneticum suite, and simulated synthetic eROSITA observations of these clusters using `PHOX` to generate the photons and the end-to-end simulator `SIXTE` to trace them through the optics and simulate the detection process. We fitted the spectra from these observations and compared the fitted temperatures and luminosities to the quantities derived from the simulations. We fitted an intrinsically scattered L_X–T scaling relation to these measurements following a Bayesian approach with which we fully took into account the selection effects and the mass function.

Results. The largest biases on the estimated temperature and luminosities of the clusters come from the inadequacy of single-temperature model fits to represent emission from multiphase gas, and from a bias arising from cluster emission within the projected r_{500c} along the line of sight but outside of the spherical r_{500c}. We find that the biases on temperature and luminosity due to the projection of emission from other clusters within r_{500c} is comparatively small. We find eROSITA-like measurements of Magneticum clusters following a L_X–T scaling relation that has a broadly consistent but slightly shallower slope compared to the literature values. We also find that the intrinsic scatter of L_X at given T is lower compared to the recent observational results where the selection effects are fully considered.

Key words. galaxies: clusters: intracluster medium – methods: numerical – X-rays: galaxies: clusters

1. Introduction

Galaxy clusters are the natural endpoints of the process of hierarchical structure formation in a Λ cold dark matter (ΛCDM) universe at the current epoch. Given their size, galaxy clusters are representative of the material properties of the universe as a whole. The mass budget of clusters is dominated by dark matter (DM), at roughly ∼80–90% of the total mass, with the remaining ∼10–20% comprised of baryons. The vast majority of these baryons reside in the diffuse ($n \sim 10^{-4}$–10^{-1} cm^{-3}) and hot ($kT \sim 1$–10 keV) ionized plasma known as the intracluster medium (ICM) that emits in the X-ray band and is visible at millimeter wavelengths via the Sunyaev–Zeldovich (SZ) effect. The stars in the galaxies and the intracluster light of stars outside of galaxies only comprise a few percent by mass.

Clusters of galaxies are important probes of cosmology, due to the fact that their number density as a function of mass and redshift is sensitive to the values of the cosmological parameters. This requires accurate mass measurements for clusters. Gravitational lensing can be used to estimate masses directly in a number of systems, but most clusters do not exhibit sufficient gravitational lensing to produce well-constrained mass models (Ramos-Ceja et al. 2022; Chiu et al. 2022). Thus, like most observed structures in the universe, the masses of galaxy clusters must typically be inferred from the kinematics of the luminous material, in this case the ICM under the assumption of hydrostatic equilibrium, using X-ray and/or SZ measurements (Bulbul et al. 2010; Ettori et al. 2019). Since computing cluster masses in this way for large cluster samples can be prohibitively expensive, scaling relations between cluster observables (such as luminosity, temperature, gas mass, or combinations of observables) and total mass computed from smaller samples can be used to estimate masses for larger samples to be used for estimating cosmological parameters (Bulbul et al. 2019; Bahar et al. 2022; Chiu et al. 2022).

The scaling relations between X-ray observables and masses are typically computed under the assumptions of hydrostatic

equilibrium and sphericity of the clusters (Gianfagna et al. 2023). Hydrostatic equilibrium is only satisfied to varying degrees in clusters, with mergers driving nonthermal gas motions (see Pratt et al. 2019, for a review). The condition of spherical symmetry is also somewhat violated, through mergers and accretion along cosmic filaments, which produces clusters with triaxial and irregular shapes (Becker & Kravtsov 2011; Lau et al. 2011).

In addition to the possible biases introduced by nonthermal pressure and asphericity, there are other potential biases introduced by multiphase gas and projection effects. The first bias comes from the fact that the ICM exhibits a range of temperatures and metallicities, though there are typically only enough counts in a low-exposure observation of a distant cluster to fit all of the emission within a particular projected radius (typically r_{500c} or r_{200c})[1] with a single-temperature and metallicity plasma emission model. These single-component models will inevitably not capture the multiphase structure of the gas, biasing the temperature and/or luminosity estimates (Peterson et al. 2003; Kaastra et al. 2004; Biffi et al. 2012; Frank et al. 2013). The second bias arises from structures that are projected in front of or behind the spherical radius of interest that nevertheless contribute to the observed emission. These structures can be associated with the cluster itself at larger radius along the sight line, or from other clusters, groups, and/or filaments projected along the sight line.

Additionally, ICM temperature is a key ingredient for cluster mass measurements from X-ray observations (e.g., Bulbul et al. 2010). In addition to calibration differences, the multiphase nature of the ICM and the structures along the line of sight may yield departing temperature measurements due to varying sensitivity of X-ray telescopes (Schellenberger et al. 2015). It is crucial to disentangle these competing effects with simulations to understand the biases in temperature and mass measurements from X-ray observations. In the context of eROSITA (Predehl et al. 2021), launched in 2019 on board the Spectrum-Roentgen-Gamma (SRG) mission (Sunyaev et al. 2021), understanding the interplay between the projection effects, multiphase nature of ICM, and calibration differences will help with the future cross-calibration work (Liu et al. 2023; Sanders et al. 2022; Iljenkarevic et al. 2022; Veronica et al. 2022; Whelan et al. 2022) and hydrostatic mass bias (Scheck et al. 2023).

In this work we address the impact of both the multiphase gas and projection biases on the cluster observables of temperature and luminosity using mock observations of galaxy clusters from the smoothed particle hydrodynamics (SPH) Magneticum Pathfinder Simulations[2] (Biffi et al. 2013, 2022; Hirschmann et al. 2014; Dolag et al. 2017). Specifically, we model the thermal emission from the hot ICM of the clusters, and pass this through an instrument model for eROSITA which includes the effects of the seven separate telescope modules (TMs), point spread function (PSF), energy-dependent effective area, spectral response, particle background, and instrument noise. We then fit single-temperature plasma models to the resulting spectra and determine the best-fit temperature and luminosity. We carry this analysis out for three separate samples of the galaxy clusters, including increasing amounts of material projected along the sight line, in order to determine the bias on the luminosity and temperature induced by the presence of these structures in the observations.

The rest of this work is structured as follows. In Sect. 2 we describe the Magneticum simulations and the cluster sample taken from them, as well as the methods used to create the synthetic X-ray observations of the clusters and fit the resulting spectra to obtain the relevant observables. In Sect. 3 we detail the results of our study. In Sect. 4 we present our conclusions.

Table 1. Redshifts and cluster numbers of simulation snapshots.

Snapshot ID	Redshift	# of clusters
124	0.174	38
128	0.137	24
132	0.101	16
136	0.066	4
140	0.033	2

2. Methods

2.1. Simulations and cluster sample

The Magneticum simulations (Hirschmann et al. 2014; Dolag et al. 2015) were run using the TreePM/SPH code P-Gadget3, an extended version of P-Gadget2 (Springel 2005). In addition to hydrodynamics, gravity, and evolution of the collisionless DM component, the simulations also include radiative cooling and heating from a time-dependent UV background, star formation and feedback, metal enrichment, and black hole growth and AGN feedback. More details about the physics implemented in the simulation can be found in Biffi et al. (2022), their Sect. 2 and references therein.

The `Box2_hr` simulation box comprises a co-moving volume of $(352\,h^{-1}\,\mathrm{cMpc})^3$ and is resolved with 2×1584^3 particles, corresponding to mass resolutions for DM of $m_{\rm DM} = 6.9\times10^8\,h^{-1}\,M_\odot$ and gas of $m_{\rm gas} = 1.4\times10^8\,h^{-1}\,M_\odot$. The simulations employ a ΛCDM cosmology with the Hubble parameter $h = 0.704$, and the density parameters for baryons, matter, and dark energy are $\Omega_{\rm b} = 0.0451$, $\Omega_{\rm M} = 0.272$, and $\Omega_\Lambda = 0.728$. The normalization of the fluctuation amplitude at 8 Mpc $\sigma_8 = 0.809$ (from the seven-year results of the Wilkinson Microwave Anisotropy Probe, Komatsu et al. 2011).

Clusters and their substructures were identified using the `SubFind` algorithm (Springel et al. 2001; Dolag et al. 2009), which employs a standard friends-of-friends algorithm (Davis et al. 1985). A total of 84 clusters were selected for this study, using a mass cut of $M_{500c} > 10^{14}\,M_\odot\,h^{-1}$, within a lightcone constructed from the simulation which has a field of view of 30×30 deg^2 and a depth of $z < 0.2$, consisting of five independent slices between $z = 0.03$ and 0.18 (see Table 1 for the redshifts of the individual snapshots and the numbers of clusters chosen from each snapshot). Slices were extracted from each corresponding output box of the Magneticum `Box2_hr` simulation by randomly shifting the pointing direction within the box. The redshift used in computing distances $z_{\rm true}$ is obtained by computing the offset of the cluster center from the center of the slice, and the redshift used in fitting spectra $z_{\rm obs}$ also takes into account the peculiar velocity of the cluster within the slice. Figure 1 shows histograms of cluster masses and redshifts from the sample. The center of each cluster is identified as the potential minimum.

[1] The overdensity radius that defines the region within which the density is 500 or 200 times the critical density of the universe.
[2] http://www.magneticum.org

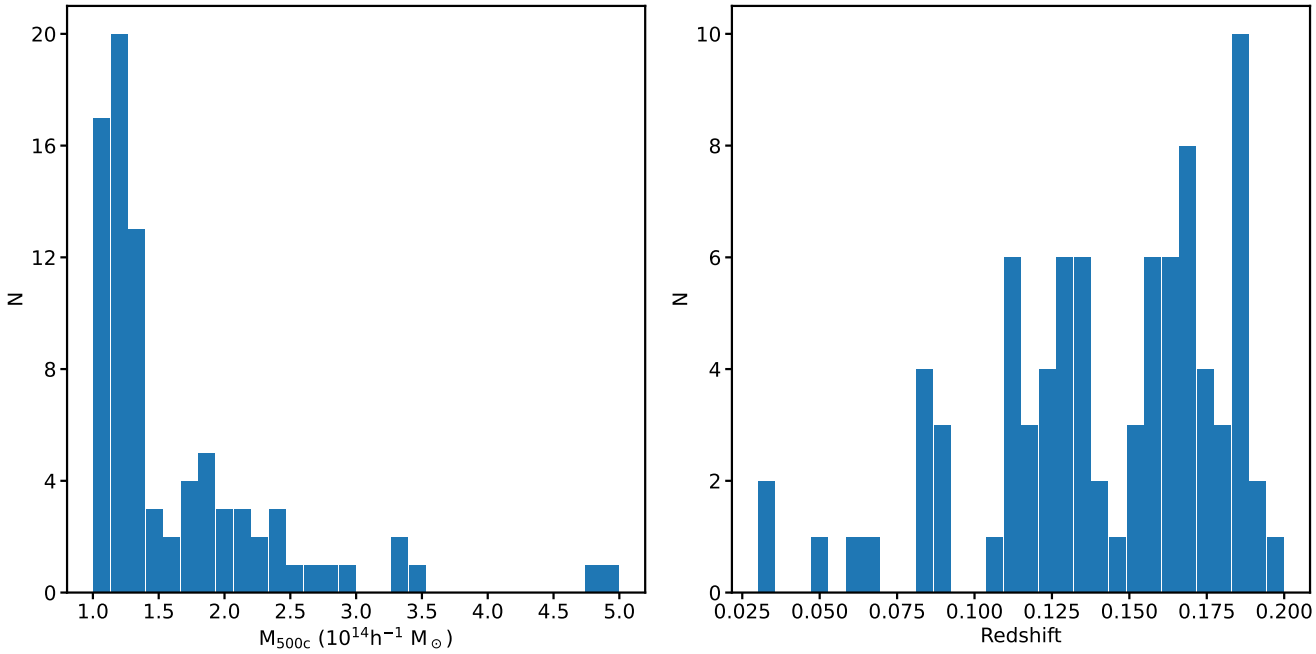

Fig. 1. Histograms of M_{500c} (left) and the redshift z_{true} for the 84 clusters in the sample.

2.2. Creating photon lists with PHOX

From our Magneticum cluster sample, we created simulated X-ray photons using the PHOX software package (Biffi et al. 2012, 2013). PHOX takes every gas particle in the simulation and computes the expected thermal X-ray spectrum from it, based on the particle's density, temperature, and abundance information. For this work, the spectra were determined using version 2.0.1 of the APEC model (Smith et al. 2001). Given the spectrum for each particle, we assumed large values for the exposure time t_{exp} and a flat effective area A_{eff} to generate a large sample of X-ray photons at the positions of the gas particles using Poisson sampling. The values of t_{exp} and A_{eff} are much larger than the values that were employed for the mock observations described in Sect. 2.3, as the observed photons were drawn from this sample based on the true t_{exp} and the effective area curve for the simulated eROSITA instrument. These photon positions are projected along a chosen line of sight, and their energies are Doppler-shifted according to the line-of-sight velocity of their originating particles. The energies are then cosmologically redshifted and a fraction of the redshifted photons are absorbed by Galactic neutral hydrogen, assuming a wabs Morrison & McCammon (1983) absorption model and setting the equivalent hydrogen column density parameter to $N_H = 10^{20}\,cm^{-2}$. The remaining photons are stored in SIMPUT[3] photon lists to be used in the instrument simulation (Sect. 2.3).

We ran PHOX on the lightcone described above. From the slices of the lightcone, we created three separate samples of photon lists. For the "isolated" sample, each cluster within the lightcone only has the photons within $2\,r_{500c}$ of the cluster potential minimum included in the sample. The "surroundings" sample includes all of the photons within the redshift slice for each cluster, and thus consists of the emission from the cluster and the structures nearest to it at the same cosmic epoch in projection. Finally, the "lightcone" sample includes the full lightcone of emission in projection, including all structures in projection within the simulated redshift range.

2.3. Creating event files with SIXTE

We generated mock eROSITA event files using the Simulation of X-ray Telescopes (SIXTE) software package (Dauser et al. 2019), version 2.7.0. Version 1.8.2 of the eROSITA instrument model was used. It is the official end-to-end simulator for eROSITA and includes all seven TMs separately. SIXTE traces the photons through the optics by using the measured PSFs and vignetting curves (Predehl et al. 2021) onto the detector. The detection process itself includes a detailed model of the charge cloud and read-out process. Specifically, we used a Gaussian charge cloud model with parameters based on ground calibration measurements (see König et al. 2022, for a recent comparison to in-flight data). In SIXTE, five of these (TMs 1, 2, 3, 4, and 6) have identical effective area curves, and TMs 5 and 7 have identical effective area curves, due to the absence of the aluminum on-chip optical light filter that is present on the other TMs (see Sect. 9.2 of Predehl et al. 2021). All seven TMs use the same redistribution matrix file (RMF) and a low-energy threshold of 60 eV.

Each SIMPUT photon list (three lists for 84 clusters) was exposed for 2 ks in pointing mode[4]. The aimpoint for each observation was set to the center of each cluster. No background events were added for any of our SIXTE simulations. The method of adding background to the spectra is detailed in Sect. 2.4.

2.4. Making and fitting spectra

From the SIXTE-produced event files, we used the HEASARC FTOOLS tool extractor (from HEASOFT v6.21) to extract a PI spectrum from each eROSITA TM. For each cluster, we

[3] http://hea-www.harvard.edu/heasarc/formats/simput-1.1.0.pdf

[4] Experiments with the toy models presented in Sect. 3.1 with the pointing and survey responses show no substantial difference between the two modes.

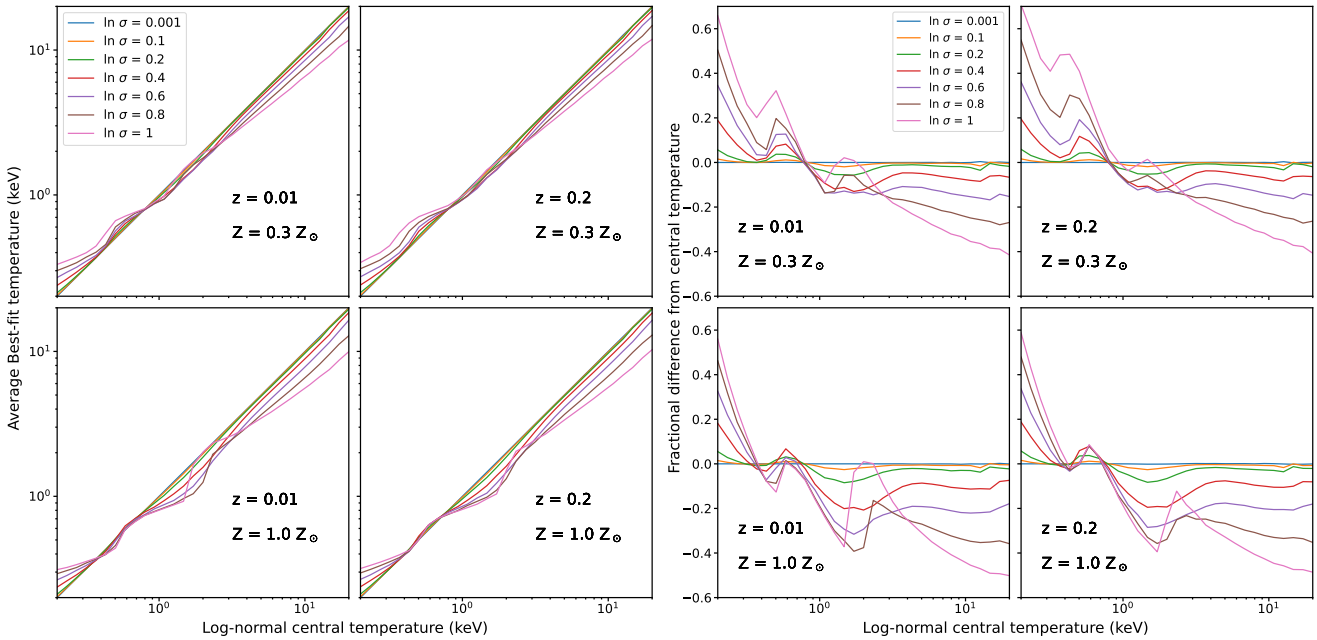

Fig. 2. Results of fitting spectra generated from log-normal temperature distributions (see Sect. 3.1). Left 2×2 panels: central temperature of distribution vs. best-fit temperature. The panels reflect variations in metallicity and redshift. Right 2×2 panels: difference in the best-fit temperature and the central temperature vs. the central temperature for the same distributions.

extracted all photons from within a circle of projected radius r_{500c} centered on the cluster potential minimum. We co-added the counts from the seven TMs into two spectra, one for each of the groups with the same effective area, as noted above.

For the background we implement two components, the cosmic X-ray background (CXB) and the particle non-X-ray background (NXB) associated with the detector. For the CXB, we assumed the form `apec+wabs*(apec+powerlaw)` and the parameters from McCammon et al. (2002). For the NXB, we employed a model comprised of a continuum with a number of emission lines added to it from Liu et al. (2022a), based on the analysis of early "filter-wheel-closed" and the eROSITA Final Equatorial Depth Survey (eFEDS) data (Brunner et al. 2022; Liu et al. 2022b; Bulbul et al. 2022). Instead of including the background events in each `SIXTE` simulation, we instead generated background PI spectra from the combined CXB+NXB model for a 2 ks exposure and the same extraction region for the source spectra and added them to the cluster spectra.

For each cluster, we fitted the spectra from the two TM groups jointly using `XSPEC`, restricting the fit to the energy range 0.4−7.0 keV, and we used the C-statistic (Cash 1979; Kaastra 2017). For the cluster emission, we used an absorbed thermal model, `wabs*apec`. We used APEC v2.0.1 in the fits, as was used in the generation of the photons. We fixed the value of the hydrogen column parameter to $N_{\rm H} = 10^{20}\,{\rm cm}^{-2}$, the same value that was used in the generation of the photon lists. We fixed the metallicity parameter to $Z = 0.3\,Z_\odot$ in the fits as it is observationally motivated that cluster metallicity averages at that value (Ezer et al. 2017; Mernier & Biffi 2022). The redshift parameter was held fixed to the redshift of the cluster determined from the lightcone, and the temperature kT and normalization parameters were left free to vary. For the background, the overall normalizations of the CXB and NXB were left free to separately vary with a Gaussian prior of 5% of the model normalization, but the rest of the background parameters were held fixed. We used the same cosmological parameters as used for the Magneticum simulation and described in Sect. 2.1. A comparison of cluster fits with and without background can be found in Appendix A. Unless otherwise noted, all quoted uncertainties are at the 1σ level.

3. Results

3.1. Toy models: Effect of multi-temperature structure on fitted temperatures

Before analyzing the temperatures of the clusters in our sample, it is instructive to explore the effect of multi-temperature structure on the results of single-temperature-model fits using simple toy models. To this end, we created idealized `apec` spectra in `XSPEC` with a log-normal temperature distribution with a central $\ln kT_0$ and a $\ln\sigma$. We simulated spectra at redshifts of $z = 0.01$ and $z = 0.2$ (bracketing the bounds of the redshift range of our cluster sample), and with metallicities of $Z = 0.3$ and $1\,Z_\odot$. The mock spectra have foreground Galactic absorption applied using the `phabs` model, for which the column density is $N_{\rm H} = 10^{20}\,{\rm cm}^{-2}$. The spectra were simulated for 40 ks with the eROSITA ARF and RMF. Each spectrum was then fit with a single absorbed `phabs*apec` model over the 0.3−7 keV band assuming no background. This process was repeated 50 times, and an average fitted temperature was taken from the sample.

Figure 2 shows the results of this procedure. The left set of 2×2 panels shows the recovered fit temperature vs. the input central temperature for a range of $\ln\sigma$ for the different redshift and metallicity options. As expected, the fitted temperature is less well recovered for larger values of $\ln\sigma$. Depending on the values of metallicity and redshift, the central temperature kT_0 is recovered most accurately for values of ∼0.5−1.5 keV. As the spread of temperatures in the distribution increases, the disagreement between the fitted temperature and the central temperature increases: it is higher for lower input temperatures and lower for higher input temperatures. This is due to the decrease in the eROSITA effective area at both low and high energies, making it more difficult to accurately constrain low and high temperatures. The right set of 2×2 panels shows the difference between

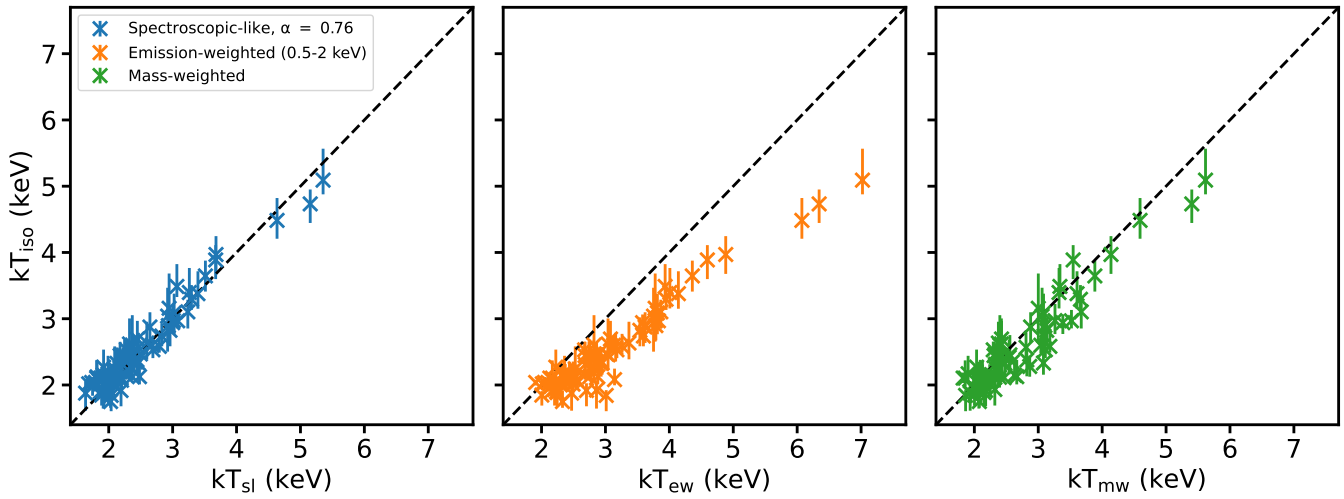

Fig. 3. Fitted temperatures from the isolated sample ($kT_{\rm iso}$) plotted against various relevant weighted temperatures. The black dashed line indicates equality between the two temperatures in each panel.

the fitted and the central temperature vs. the central temperature. For $\ln\sigma \leq 0.2$, the relative error is less than ∼5% for all temperatures in the range 0.2−20 keV. The error at temperatures $0.4 \lesssim kT_0 \lesssim 1$ keV is ≲20% for $\ln\sigma \leq 0.6$, but is ∼30% for higher values. For lower temperatures and higher values of $\ln\sigma$, the fractional error can increase to ∼50−60%. At temperatures $kT_0 \gtrsim 1$ keV, the fractional errors increase with increasing temperature, down to a ∼20% decrease for $\ln\sigma \leq 0.6$, and down to a ∼50% decrease for $\ln\sigma \leq 1$. In general, the errors at higher temperatures ($kT_0 \gtrsim 1$ keV) are larger for higher redshifts and higher metallicities.

3.2. Cluster temperatures

3.2.1. Comparison of fitted temperatures with simulation temperatures

We begin the analysis of the cluster mocks by comparing the fitted spectral temperatures from the mock eROSITA observations to cluster temperatures determined from the simulation data with different weightings. For this, we use the fitted temperatures $kT_{\rm iso}$ from the isolated sample to determine a spectroscopic-like temperature, employing the method of Mazzotta et al. (2004, hereafter M04). The general idea is that the temperature estimated via spectral fitting can be approximated by a weighting of the form

$$T_{\rm sl} = \frac{\int wT\,{\rm d}V}{\int w\,{\rm d}V}, \tag{1}$$

where the weighting function is[5]

$$w = n_{\rm e}n_{\rm p}T^{-\alpha}. \tag{2}$$

Here T is the temperature of each SPH particle, and $n_{\rm e}$ and $n_{\rm p}$ are the electron and proton densities, respectively. For *Chandra* and *XMM-Newton* observations, M04 found a best-fit value of $\alpha \approx 0.75$. Since the effective area of eROSITA is different from *Chandra* and *XMM-Newton*, we cannot simply assume the same value of α, but instead must determine it via a similar procedure.

[5] In M04 the weighting is $\propto T^{\alpha-3/2}$, whereas in our case we absorb the $-3/2$ into the definition of α, and change the sign of the exponent so that $\alpha > 0$.

To do this, we first compute $T_{\rm sl}$ from Eq. (1) for each of the clusters in our sample within a cylinder of radius $r_{\rm 500c}$, centered on the cluster potential minimum and extended along the line of sight (using only the gas particles as belonging to the cluster as identified by the `SubFind` algorithm), for a range of α values. We use a cylinder instead of a sphere with radius $r_{\rm 500c}$ since the spectrum that is fitted includes emission from along the entire line of sight within the projected angular radius corresponding to $r_{\rm 500c}$. Then, following a similar procedure to M04, we determine the relative error in $T_{\rm sl}$, summed over all of the clusters:

$$\Delta(\alpha) = \frac{1}{N}\sqrt{\sum_i\left(\frac{T_{{\rm sl},i} - T_{{\rm iso},i}}{T_{{\rm iso},i}}\right)^2}. \tag{3}$$

We then minimize $\Delta(\alpha)$ to find a best-fit value of $\alpha = 0.76^{+0.05}_{-0.04}$. Error bars on α were determined by re-sampling 1000 different values of the fitted temperature for each cluster in the isolated sample, fitting for α for each of the 1000 samples, and finding the 68% confidence limit. This value is consistent within the 1σ errors to that found for *Chandra* and *XMM-Newton* temperatures from M04.

Figure 3 shows $kT_{\rm iso}$ plotted against the spectroscopic-like temperature $kT_{\rm sl}$, the emission-weighted temperature $kT_{\rm ew}$ in the 0.5–2 keV band, and the mass-weighted temperature $kT_{\rm mw}$. Each temperature measure is computed for each cluster directly from the simulation data. The leftmost panel shows $kT_{\rm iso}$ versus $kT_{\rm sl}$ with $\alpha = 0.76$. Despite the simplicity of this formula, the relation represents reasonably well the distribution of fitted temperatures with a mean difference between $kT_{\rm iso}$ and $kT_{\rm sl}$ of ∼0.05 keV (∼3%) and a standard deviation of 0.18 keV (∼8%; see also Table 2). The value of $kT_{\rm ew}$ (center panel) trends higher than the fitted spectroscopic temperature, especially at temperatures emitting most strongly in rest-frame energies ≳2 keV where the sensitivity of eROSITA decreases. Even though the 0.5−2 keV band is covered well by eROSITA's effective area, the clusters at higher temperatures which only contribute photons at the higher end of this band are downweighted in the best-fit temperatures compared to the emission-weighted temperatures. The same underestimate in best-fit temperature is also seen in the comparison to $kT_{\rm mw}$ (right panel), though not as severely.

Figure 4 shows $kT_{\rm iso}$ plotted against $kT_{\rm sl}$ again (left panel), along with the difference between the two temperatures $kT_{\rm iso}$ −

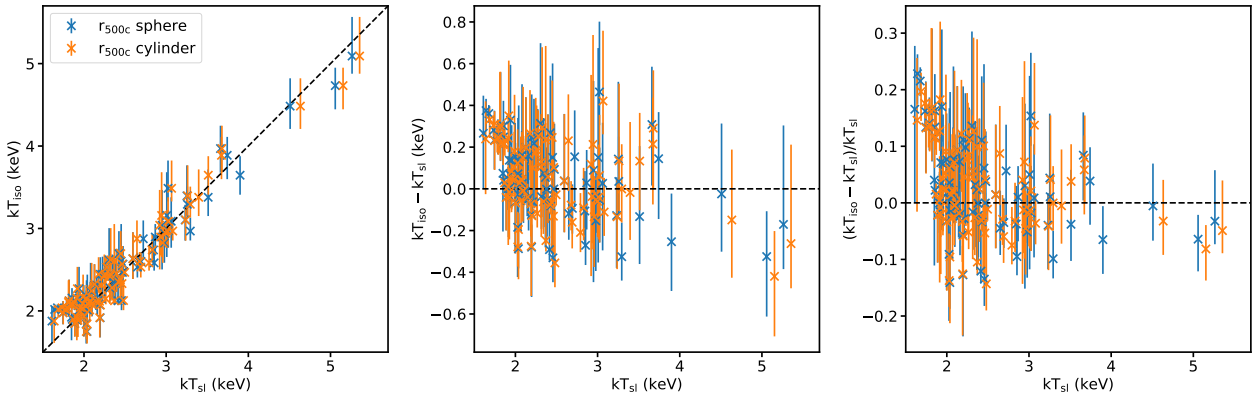

Fig. 4. Spectroscopic-like temperatures computed from simulation (using Eq. (1)), using both the sphere and cylinder regions vs. fitted temperatures from the isolated sample. The center panel shows the differences between the two temperatures plotted against the spectroscopic-like temperatures, and the right panel shows the fractional difference against the spectroscopic-like temperatures. The black dashed lines indicate equality between the temperatures in each panel.

Table 2. Mean and standard deviation in differences between fitted quantities and simulations.

	$kT_{\rm iso} - kT_{\rm sl}$ sphere/cylinder (keV)	$(L_{\rm iso} - L_{\rm sim})E(z)^{-1}$ sphere/cylinder (10^{44} erg s^{-1})
Mean	0.05/0.05	0.030/–0.006
Std. dev.	0.18/0.18	0.036/0.032
Mean %	2.7/2.9	6.3/–2.3
Std. dev. %	7.9/7.8	4.6/5.1

$kT_{\rm sl}$ plotted against $kT_{\rm sl}$ (center panel), and the fractional difference $(kT_{\rm iso} - kT_{\rm sl})/kT_{\rm sl}$. In this figure we also show the effect of computing $kT_{\rm sl}$ using all of the gas particles within a sphere of radius r_{500c} centered on the cluster potential minimum (blue points) in addition to the temperatures computed from the cylindrical regions. The latter is more representative of what is measured by the spectral fitting, since everything is included in projection within the aperture of r_{500c}. For both cases, most of the differences between the two temperatures fall between ±0.4 keV, or ±20%. The overall distributions of the temperatures measured within the spheres or the cylinders are very similar (Fig. 4 and Table 2), though the power-law index in Eq. (2) for the spherical case is $\alpha = 0.85^{+0.05}_{-0.03}$, roughly 2σ away from the value of $\alpha = 0.76$ computed for the cylindrical regions. The overall similarity between the two temperatures reflects the fact that it is dominated by the gas with higher emission measures ($\propto n^2$) near the cluster centers, which will be similarly captured by either the cylindrical or spherical regions.

It can be seen from the center panel of Fig. 4 that the errors in $kT_{\rm sl}$ skew slightly toward lower best-fit temperatures at higher $kT_{\rm sl}$. This same trend in all four temperature measures from Figs. 2 and 3 is consistent with the results of Sect. 3.1. Table 2 shows the mean and standard deviation of $kT_{\rm iso} - kT_{\rm sl}$, which are relatively small. However, M04 advised that for *Chandra* and *XMM-Newton* spectra the simple formula for $kT_{\rm sl}$ is accurate up to several percent only for temperatures of $kT \gtrsim 3$ keV, where the spectrum is dominated by continuum emission. Vikhlinin (2006) showed that for $kT \lesssim 3$ keV a more complicated (and non-analytic) algorithm for determining $kT_{\rm sl}$ was required for these line-dominated spectra. Most of our sample lies in this lower-temperature range, which is compounded by the fact that eROSITA is more sensitive at lower X-ray energies, ensuring that our cluster spectra are mostly dominated by line emission from metals. For this reason, the simple power-law prescription in our case is less accurate, with a standard deviation of ∼8% (Table 2) and maximum deviations of ∼±20% (right-most panel of Fig. 4), especially at lower temperatures which are the most line-dominated. We save a treatment similar to Vikhlinin (2006) for eROSITA spectra for future work.

We can also compare the fitted temperatures $kT_{\rm iso}$ and their differences from the expected temperature from the simulation to the results of the toy models in Sect. 3.1. To do this, we compute the sample mean $\ln kT_0$ and the sample standard deviation $\ln \sigma$ from the SPH particles in each cluster, weighted by the emission measure. The former allows us to make a comparison to the fractional difference of the fitted temperature from the central temperature from the toy models directly. This is shown in Fig. 5. The bands show the range of fractional differences from all four combinations of metallicity and redshift from Fig. 2, for several values of $\ln \sigma$. The points show the values of the fractional difference computed for the 84 clusters, where the colors of the points are coded according to the value of $\ln \sigma$ they are closest to (within $\Delta \ln \sigma = 0.1$).

There is no precise correspondence between the values from the clusters and the toy models, nor should one be expected since the cluster gas temperatures do not necessarily follow a log-normal distribution. However, there is at least qualitative agreement between them. For most of the 84 clusters, $\ln \sigma \approx 0.6$ (green points). For most of the clusters, the fitted temperature $kT_{\rm iso}$ underestimates the central temperature kT_0 by ∼10–20%, in general agreement with the predictions of the toy models.

3.2.2. Effect of cosmic structure on the observed cluster temperatures

Other structures aligned with our observed clusters in projection will bias the observed temperature of the cluster. Figure 6 shows the differences between the isolated sample and the surroundings

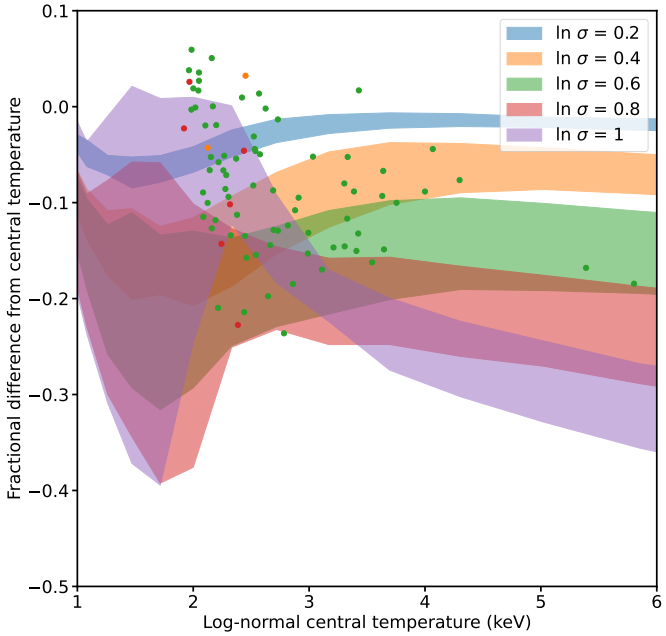

Fig. 5. Fractional difference of the fitted temperature from the log-normal central temperature kT_0 from the toy models and the 84 clusters from the simulation. The bands show the range of values for the four different combinations of redshift and abundance from the toy models described in Sect. 3.1. The points show the values computed from the clusters, where $\ln kT_0$ and $\ln \sigma$ were computed using sample means and variances weighted by the emission measure of the SPH particles. The points are color-coded according to the value of $\ln \sigma$ they are closest to (within $\Delta \ln \sigma = 0.1$).

and lightcone samples, plotted against the temperatures from the isolated sample. The temperatures of the surroundings and lightcone samples in general track the isolated sample very closely, all well within the measurement errors. Table 3 shows the mean and standard deviation of ΔkT for each of the two comparisons shown in Fig. 6. The mean difference in all three samples is very small, with an absolute value ≤ 0.02 keV in all cases. The standard deviation of the differences between the samples is also very small, $\sigma_{\rm kT} \approx 0.04-0.06$ keV.

3.3. Cluster luminosities

3.3.1. Comparison of fitted luminosities with simulation luminosities

The luminosities of the clusters from the simulation can be directly compared to the luminosities estimated from the spectral fitting. The left panel of Fig. 7 shows the X-ray luminosity in the 0.5−2.0 keV band determined from the best-fit model for each cluster in the isolated sample vs. the computed luminosity in the same band from the SPH particles within a sphere of radius of r_{500c}. The luminosity is computed in PHOX using the same methods used to compute the spectrum for each SPH particle as described in Sect. 2.2, but without including the effects of Poisson statistics. The right panel of the same figure shows the difference between the fitted luminosity and the simulation luminosity $L_{\rm iso} - L_{\rm sim}$, for both the sphere and cylinder regions mentioned above. Here, unlike the temperatures in Sect. 3.2.1, the difference between the fitted luminosity and the simulation luminosity depends very clearly on the region chosen. The fitted luminosity overestimates the luminosity in the spherical regions by ∼6%, due to the fact that the former includes material outside of the spherical radius of r_{500c} along the sight line. The fitted luminosity is in much better agreement with the luminosity in the cylindrical regions, as expected, with a mean difference of ∼−2%. In both cases the standard deviation of the luminosity differences is ∼5%. A similar luminosity bias from a projected measurement over that expected from a spherical region was noted by Dolag et al. (2006), who also found a similar overestimate of less than ∼10% (see the discussion in their Sect. 5.2).

Aside from this bias in the luminosity related to geometrical effects, another fundamental limitation is that of fitting a single-component temperature and abundance model to a plasma which is inherently multi-temperature and with varying chemical composition. The best-fit single-component model will necessarily only capture a portion of the expected luminosity, depending on how much the plasma differs from a single phase. In addition, as mentioned above, in the fits the metallicity parameter is held fixed at $Z = 0.3\,Z_\odot$, which is a typical value outside of the core region of clusters. The typical number of counts in a 2 ks spectrum for any of our clusters do not provide sufficient statistics to constrain the metallicity. The metallicity in the cores of clusters is typically higher, which could lead to an underestimate in the luminosity.

3.3.2. Effect of cosmic structure on the observed cluster luminosities

Substructures in projection with observed clusters bias the estimated luminosity upward. Therefore, it is expected that the surroundings and lightcone samples can have higher luminosities than the isolated sample.

Figure 8 shows comparisons between the luminosities of the clusters from the isolated sample versus the surroundings and lightcone samples in terms of the difference ΔL between the samples on the y-axis. Most of the differences between the isolated sample and the surroundings and lightcone samples are very minor, but there are several clusters for which the increase in luminosity due to projected structures is somewhat significant (∼5−20%). The number of these clusters with significant deviations is larger in the lightcone sample, as expected. Overall, however, the mean difference is very small, with very low scatter (∼2−3%), as seen in Table 3.

It is also instructive to examine the differences in temperature and luminosity between the samples together. This is shown in Fig. 9, which plots the differences in luminosity versus temperature between the isolated sample and the other two. As already seen, most clusters lie very close to the point of no significant difference in either temperature or luminosity together, but there is a trend of a small subset of clusters with higher luminosity and lower temperature (going up and to the left in both panels of Fig. 9), which is more statistically significant in luminosity than temperature. This effect is more pronounced in the difference between lightcone and isolated samples. The overall effect is readily attributed to the fact that the densest gas in clusters in general has cooled in the cores, so that any bright substructure in projection that makes a significant increase in apparent brightness is also likely to make the target cluster appear cooler than it actually is.

3.4. Largest differences between the samples

We now look at the clusters that have the largest differences in fitted temperature and luminosity between the samples from Sects. 3.2.2 and 3.3.2 and visually inspect them. We note that here we also inspect differences between the surroundings and

Table 3. Mean and standard deviation in changes to observed temperature and luminosity between samples.

	$kT_{\rm surr} - kT_{\rm iso}$ (keV)	$kT_{\rm lc} - kT_{\rm iso}$ (keV)	$(L_{\rm surr} - L_{\rm iso})E(z)^{-1}$ (10^{44} erg s^{-1})	$(L_{\rm lc} - L_{\rm iso})E(z)^{-1}$ (10^{44} erg s^{-1})
Mean	–0.011	–0.019	0.0026	0.0064
Std. dev.	0.045	0.062	0.0079	0.0095
Mean %	–0.4	–0.7	0.7	1.7
Std. dev. %	1.7	2.3	2.4	3.0

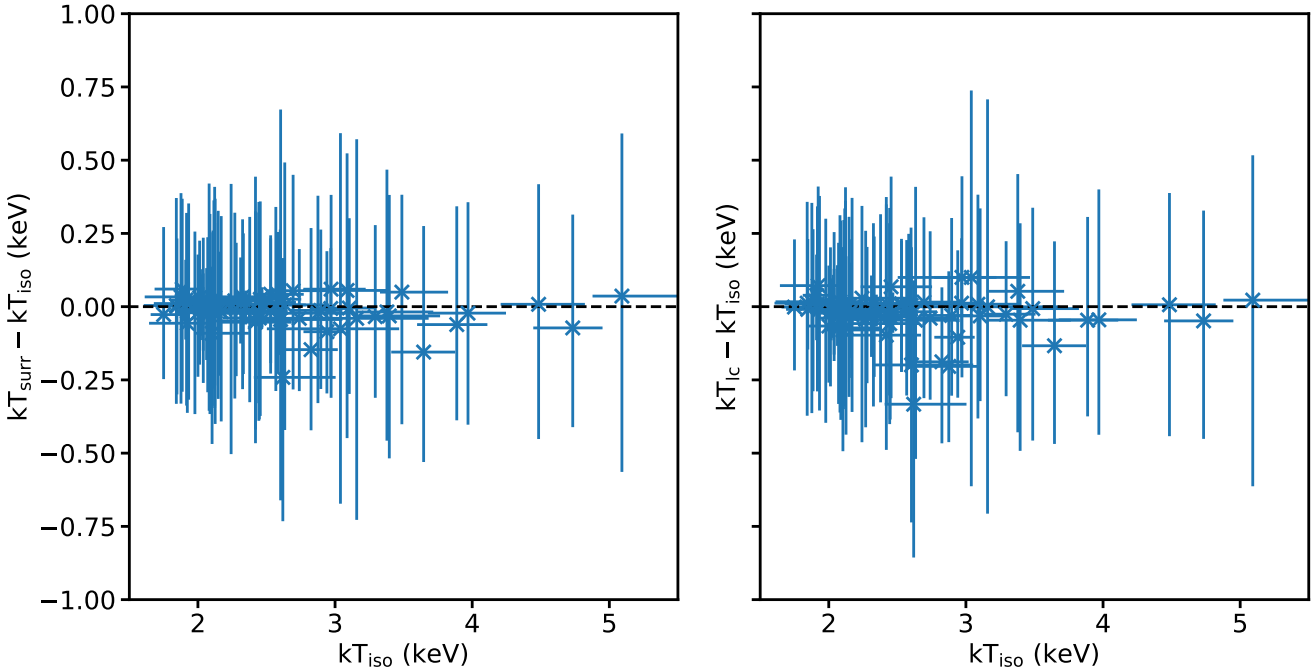

Fig. 6. Comparisons between fitted cluster temperatures of the isolated sample vs. the surroundings and lightcone samples. Shown are the difference of two samples plotted against the isolated sample (where the black dashed line indicates no difference).

lightcone samples, unlike the previous sections. We show these five clusters (we do not show the largest negative luminosity differences between the samples since these are very small, which is expected since we do not expect the addition of substructure to bias the luminosity lower):

– snapshot 128, halo ID 231 has the highest $(kT_{\rm surr} - kT_{\rm iso})/kT_{\rm iso} = 3.2\%$ at $kT_{\rm iso} = 1.89$ keV;
– snapshot 128, halo ID 241 has the highest $(kT_{\rm lc} - kT_{\rm surr})/kT_{\rm surr} = 6.9\%$ at $kT_{\rm surr} = 1.87$ keV;
– snapshot 128, halo ID 46 has the lowest $(kT_{\rm surr} - kT_{\rm iso})/kT_{\rm iso} = -9.2\%$ at $kT_{\rm iso} = 2.62$ keV and the highest $(L_{\rm surr} - L_{\rm iso})/L_{\rm iso} = 17.8\%$ at $L_{\rm iso}E(z)^{-1} = 0.256 \times 10^{44}$ erg s^{-1};
– snapshot 132, halo ID 91 has the lowest $(kT_{\rm lc} - kT_{\rm surr})/kT_{\rm surr} = -6.4\%$ at $kT_{\rm surr} = 2.85$ keV;
– snapshot 124, halo ID 135 has the highest $(L_{\rm lc} - L_{\rm surr})/L_{\rm surr} = 11.8\%$ at $L_{\rm surr}E(z)^{-1} = 0.208 \times 10^{44}$ erg s^{-1}.

We show the mock cluster images (without background) in Figs. 10–14. All detected events are shown. In all of these cases, there is obvious bright substructure that appears within or near the aperture of r_{500c} that biases the temperature and/or luminosity. In many cases, such bright substructures may be easily masked to avoid such a luminosity or temperature bias. However, for all of these extreme cases the differences are very small, and for the temperatures are all within the measurement errors.

3.5. Luminosity–temperature relation

3.5.1. *L–T* relation: Introduction and methodology

The interconnection of the physical properties of clusters is described by scaling relations. Kaiser (1986) derived simple forms of these relations, which are called self-similar scaling relations, by assuming gravity to be dominant during the formation and evolution of clusters. However, it is nontrivial to derive precise forms of these relations because gravity is not the only dominant process that is regulating the formation and evolution of these objects, but there are other complex baryonic processes, such as AGN feedback, that alter the physical properties and therefore the scaling relations (Puchwein et al. 2008). This alteration naturally gives rise to the need for the calibration of these relations using simulations and observations. There are many studies in the literature that show the employed sample selection method and how the criteria may introduce a large bias to the calibrated scaling relations if the selection effects are not properly taken into account (see Mantz 2019, for examples and discussion). Therefore, modeling and calibrating scaling relations go hand in hand with the modeling of the selection and the abundance of the objects as a function of the physical properties of interest.

One of the most affected relations from the nonthermal baryonic processes is the X-ray luminosity-temperature ($L_{\rm X}$–T)

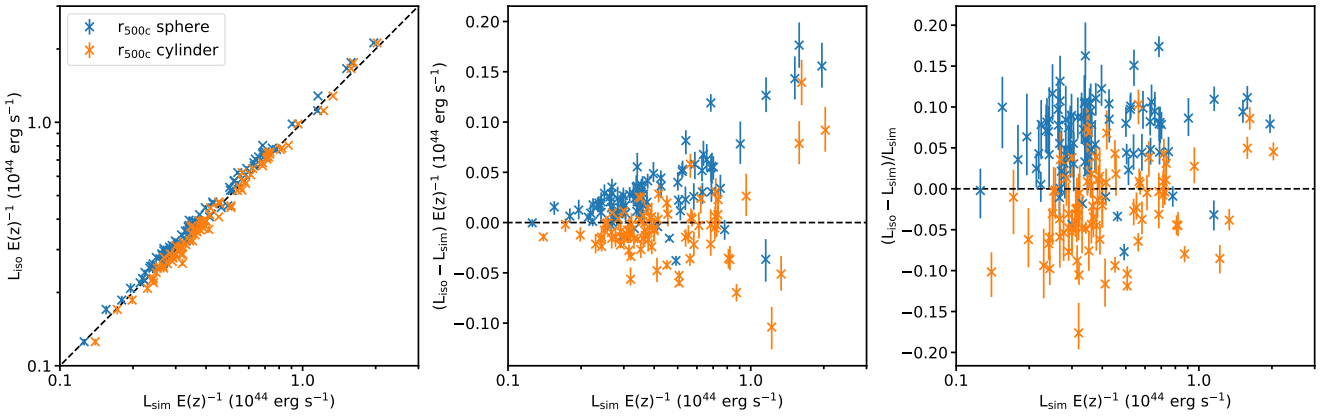

Fig. 7. Cluster luminosities computed from the simulation vs. the fitted luminosities from the isolated sample. The right panel shows the differences between the two luminosities plotted against the simulation luminosity. The black dashed lines indicate equality between the luminosities in each panel.

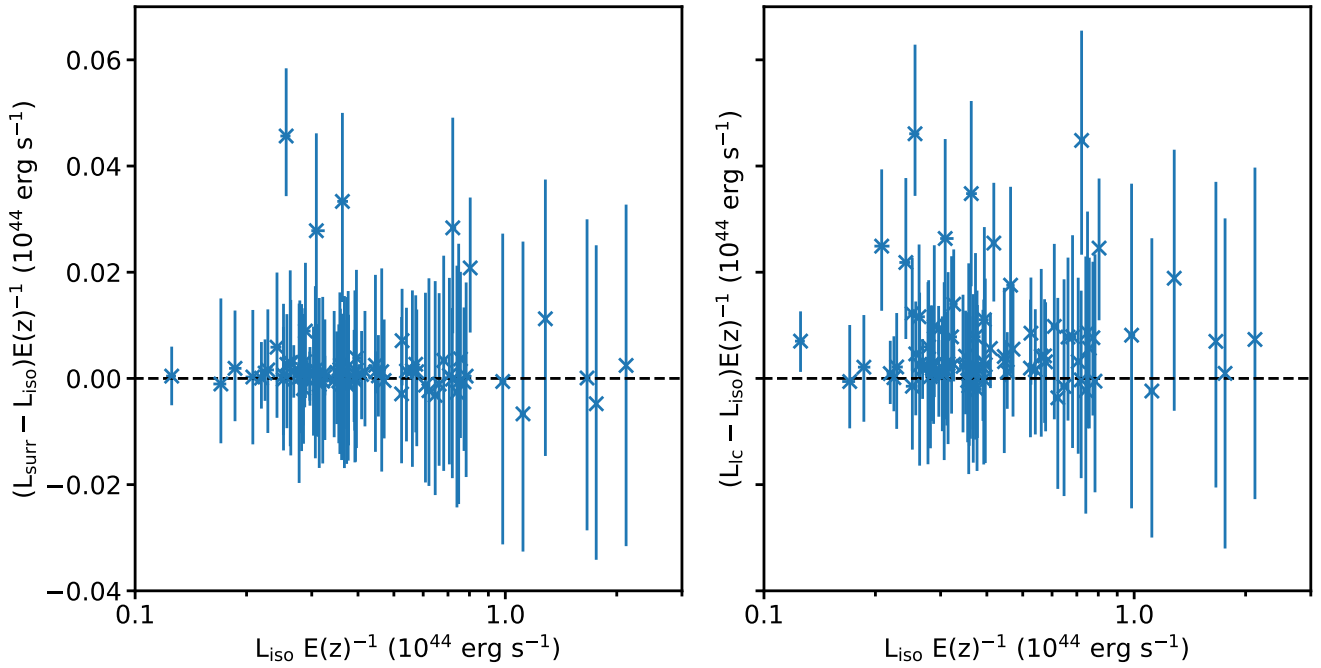

Fig. 8. Comparisons between the fitted cluster luminosities of the isolated sample vs. the surroundings and lightcone samples, showing the difference of two samples plotted against the isolated sample (where the black dashed line indicates no difference).

relation. This is due to the fact that these observables have a strong dependence on the distribution and the average kinetic energy of the hot ICM that are modified directly by the non-thermal processes. These observables can also be affected by the presence (or absence) of cool cores (Mantz et al. 2018; Maughan 2007). L_X and T are the two main X-ray observables, and therefore there are a large number of observational studies trying to constrain the L_X–T relation (e.g., Pratt et al. 2009; Eckmiller et al. 2011; Maughan et al. 2012; Lovisari et al. 2015; Kettula et al. 2015; Zou et al. 2016; Giles et al. 2016; Bahar et al. 2022).

In this work we fit the L_X–T relation for the three samples, namely isolated, surroundings, and lightcone, using the same statistical framework. By doing this, we put constraints on the underlying L_X–T relations of the Magneticum simulations for these three samples by fully simulating the observation and fitting pipeline as if this were an observational scaling relation calibrations study. We compare the results for different samples with each other in order to quantify the impact of the surrounding and in-projection structure on the L_X–T relation. Moreover, we compare our best-fit relations with the previously reported L_X–T scaling relation results to quantify where L_X–T relation of eROSITA-like observables of Magneticum clusters lie compared to other observational and simulation findings.

We followed a Bayesian approach in order to fit the relations for the three samples. In the fitting of the three samples, we used the same statistical framework where we fully take into account the selection effects and the mass function. The Bayesian framework we employed here is a modified version of the one used in Bahar et al. (2022).

The cluster sample used in this work is selected by applying a mass cut of $M_{500c} > 10^{14}\,M_\odot\,h^{-1}$ (see Sect. 2.1). This is different from the usual X-ray-selected samples that are most commonly used for calibrating the L_X–T relation, such as the

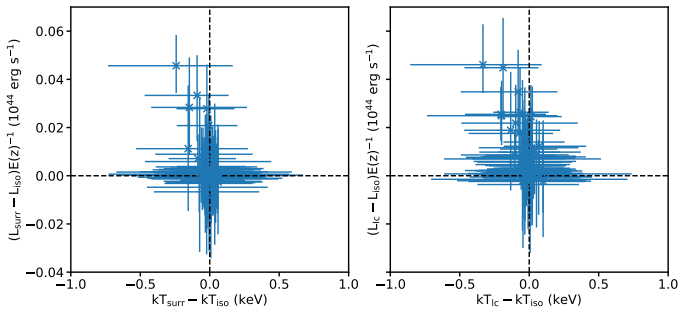

Fig. 9. Comparisons of differences between the isolated sample and the surroundings and lightcone samples in temperature vs. luminosity of the three different samples. The black dashed lines indicate there is no difference between the two samples.

eFEDS sample (Liu et al. 2022b; Bahar et al. 2022) or the XXL sample (Pacaud et al. 2016; Giles et al. 2016). In our framework the effect of sample selection is taken into account by jointly modeling the L_X−T and T−M_{500c} relations, with priors on the T−M_{500c} relation, and marginalizing over the selection observable M_{500c}.

The statistical description of this framework is as follows. The joint probability function as a function of the observed ($\hat{L}_X$, $\hat{T}$) and true (L_X, T, M_{500c}) observables is given by

$$P(\hat{L}_X, \hat{T}, L_X, T, M_{500c}, I|\theta, z) = P(I|M_{500c}, z)P(\hat{L}_X, \hat{T}|L_X, T) \times P(L_X, T|M_{500c}, \theta, z)P(M_{500c}|z), \quad (4)$$

where $P(I|M_{500c}, z)$ is the selection function, which is defined as the probability of the cluster with a given M_{500c} and z being included (I) in the cluster sample; $P(\hat{L}_X, \hat{T}|L_X, T)$ is the probability distribution of the measurement uncertainties of the L and T observables including the covariance between them; $P(L_X, T|M_{500c}, \theta, z)$ is the modeled scaling relation between L_X−T and T−M_{500c} with free parameters θ; and $P(M_{500c}|z)$ is the mass function.

We modeled the scaling relation term $P(L_X, T|M_{500c}, \theta, z)$ as a bivariate normal distribution in the logarithmic L_X−T−M space as

$$P(\log(L_X), \log(T)|\log(M_{500c}), \theta, z) = \mathcal{N}(\boldsymbol{\mu}, \boldsymbol{\Sigma}), \quad (5)$$

where the mean is

$$\boldsymbol{\mu} = \begin{bmatrix} \log(L_X) = \log\left(A_{lt}\ L_{X,piv}\left(\frac{T}{T_{piv}}\right)^{B_{lt}}\left(\frac{E(z)}{E(z_{piv})}\right)^{C_{lt}}\right) \\ \log(T) = \log\left(A_{tm}\ T_{piv}\left(\frac{M_{500c}}{M_{500c,piv}}\right)^{B_{tm}}\left(\frac{E(z)}{E(z_{piv})}\right)^{C_{tm}}\right) \end{bmatrix}, \quad (6)$$

and the covariance matrix is

$$\boldsymbol{\Sigma} = \begin{bmatrix} \sigma^2_{L_X|T} & \rho\ \sigma_{L_X|T}\ \sigma_{T|M_{500c}} \\ \rho\ \sigma_{L_X|T}\ \sigma_{T|M_{500c}} & \sigma^2_{T|M_{500c}} \end{bmatrix}. \quad (7)$$

The quantity θ in Eq. (5) includes the nine free parameters in Eqs. (6) and (7) which are, A_{lt}, B_{lt}, C_{lt}, A_{tm}, B_{tm}, C_{tm}, $\sigma_{L_X|T}$, ρ, and $\sigma_{T|M_{500c}}$. The parameters $L_{X,piv}$, T_{piv}, $M_{500c,piv}$, and z_{piv} in Eq. (6) are the pivot values of the corresponding observables. For $L_{X,piv}$ and T_{piv} we used the median of the measured values of the sample as the pivot value. For $M_{500c,piv}$ and z_{piv} we used the median true value that we obtained from the simulation. The summary of the pivot values used in this work is provided in Table 4.

With our mass selected sample, the selection function term $P(I|M_{500c}, z)$ in Eq. (4) simply becomes a unit step function, which can be formulated as

$$P(I|M_{500c}, z) = H(M_{500c}) = \begin{cases} 0 & M_{500c} \leq 10^{14}\ M_\odot\ h^{-1} \\ 1 & M_{500c} > 10^{14}\ M_\odot\ h^{-1} \end{cases}. \quad (8)$$

Lastly, for the mass distribution term, $P(M_{500c}|z)$, we used the Tinker et al. (2008) mass function.

After modeling all the terms in the joint probability density function, we marginalize over the Eq. (4) nuisance variables (L_X, T, M_{500c}) in order to get the likelihood of the measured observables ($\hat{L}_X$, $\hat{T}$). This gives us an initial likelihood for a single cluster of the form

$$P(\hat{L}_X, \hat{T}, I|\theta, z) = \int\int\int_{L_X,T,M_{500c}} P(I|M_{500c}, z)P(\hat{L}_X, \hat{T}|L_X, T) \times P(L_X, T|M_{500c}, \theta, z)P(M_{500c}|z)\mathrm{d}L_X\mathrm{d}T\mathrm{d}M_{500c}. \quad (9)$$

Given the initial form of the likelihood, we use the Bayes theorem to get the conditional likelihood of having $\hat{L}_{X,i}$ and $\hat{T}_i$ measurements. Since the cluster is detected, it is at a redshift of z_i and the trial scaling relations parameters are θ. This gives us the final likelihood for a single cluster of the form

$$\mathcal{L}(\hat{L}_{X,i}, \hat{T}_i|I, \theta, z_i) = \frac{P(\hat{L}_{X,i}, \hat{T}_i, I|\theta, z_i)}{\int\int P(\hat{L}_{X,i}, \hat{T}_i, I|\theta, z_i)\mathrm{d}\hat{L}_{X,i}\mathrm{d}\hat{T}_i} = \frac{P(\hat{L}_{X,i}, \hat{T}_i, I|\theta, z_i)}{P(I|z_i)}. \quad (10)$$

Lastly, we multiply the final form of the likelihood for each cluster to get the overall likelihood of the sample. This gives us a likelihood of the form

$$\mathcal{L}(\hat{L}_{X,all}, \hat{T}_{all}|I, \theta, z) = \prod_i^{\hat{N}_{det}} \mathcal{L}(\hat{L}_{X,i}, \hat{T}_i|I, \theta, z_i), \quad (11)$$

where $\hat{L}_{X,all}$ and $\hat{T}_{all}$ are the measured values of the L_X and T observables for all clusters and $\hat{N}_{det}$ is the number of clusters in our sample.

We note that the denominator in Eq. (10) does not depend on the model parameters (θ) and therefore is a constant in our Bayesian framework. For this reason, it is not necessary to calculate it over and over again for each likelihood iteration.

We fit all three L_X−T relations, isolated, surroundings, and lightcone, one for each sample, using this likelihood. We sampled the likelihood using the MCMC sampler package `emcee` (Foreman-Mackey et al. 2013) where we used flat priors for the A_{lt}, B_{lt}, C_{lt}, and $\sigma_{L_X|T}$ parameters and Gaussian priors for A_{tm}, B_{tm}, and C_{tm}, in the shape of the posterior distributions obtained in Chiu et al. (2022) for the T−M_{500c} relation and a tight Gaussian prior around 0.2 for $\sigma_{T|M_{500c}}$, which is the intrinsic scatter value of the simulated clusters in our sample. For the priors of the T−M_{500c} relation, we used observationally calibrated Chiu et al. (2022) results rather than the intrinsic T−M_{500c} relation of the clusters in Magneticum simulation. Our aim in doing this is to emulate the real-life scenario the best we can, where the universe is observed with eROSITA without having access to the intrinsic T−M_{500c} relation from the simulation. The list of priors for each free parameter is provided in Table 5.

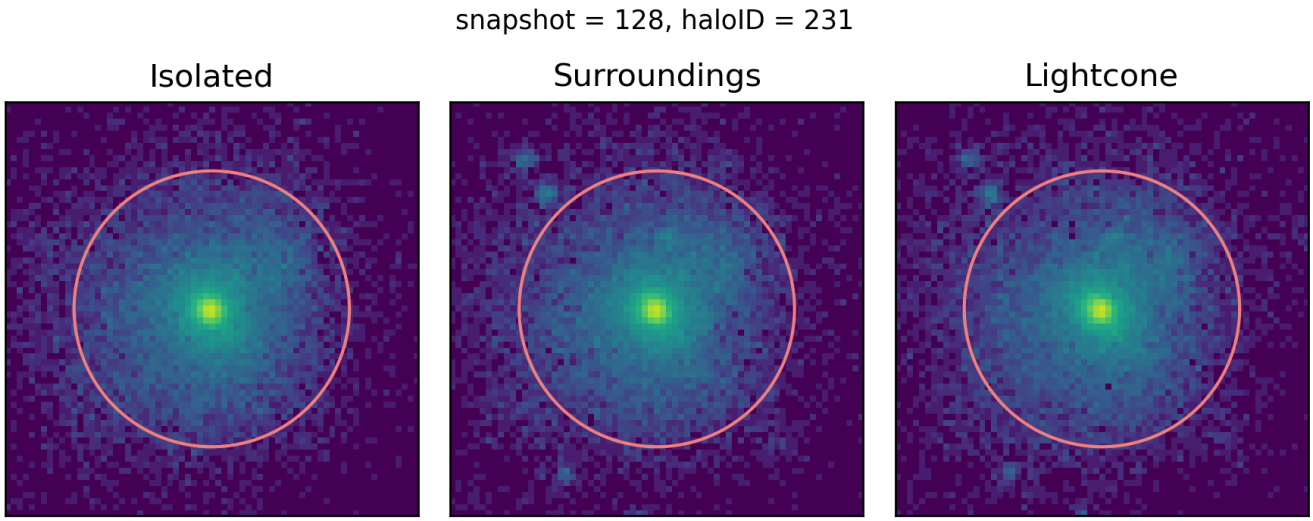

Fig. 10. Mock eROSITA image of the cluster in snapshot 128 with halo ID 231. It has the highest $(kT_{\rm surr} - kT_{\rm iso})/kT_{\rm iso}$. All events are shown, and no background is included in the image. The circle indicates a radius of $r_{\rm 500c}$.

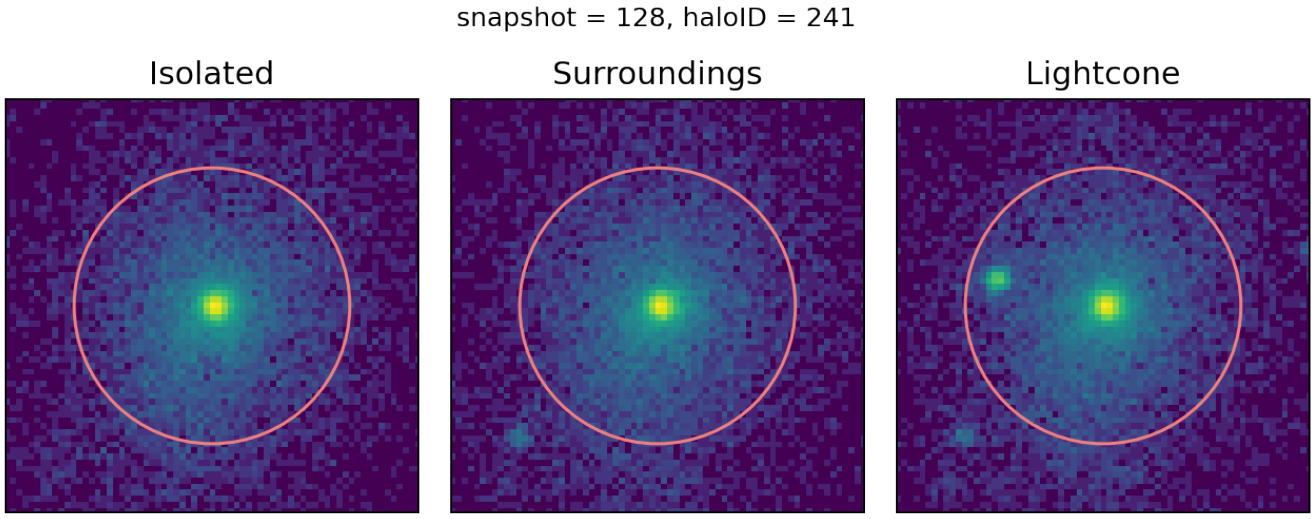

Fig. 11. Mock eROSITA image of the cluster in snapshot 128 with halo ID 241. It has the highest $(kT_{\rm lc} - kT_{\rm surr})/kT_{\rm surr}$. All events are shown, and no background is included in the image. The circle indicates a radius of $r_{\rm 500c}$.

3.5.2. *L*–*T* relation: Results and comparison with observations

As a result of our Bayesian fitting procedure, for each sample, we obtained posterior distributions for the nine free parameters. We present best-fit scaling relation parameters of Magneticum clusters measured through an eROSITA-like pipeline in Table 6. We do not observe large variations between the results of different samples. This is expected since the measurement differences between the samples are not very large compared to the error bars. This results in the measurement differences between different samples having a mild effect on the final best-fit values that is taken into account as intrinsic scatter of the relation. The lightcone sample includes the full X-ray emission in projection, and therefore the observables measured for the lightcone sample are the ones that are the closest to the actual eROSITA measurements (see Sect. 2.2). Accordingly, for comparison with the literature, the best-fit results of the lightcone sample should be used. The best-fitting scaling relation model to the $L_{\rm X}$ and T measurements of the lightcone sample and the posterior distribution of the parameters can be found in Fig. 15. The self-similar prediction for the $L_{\rm X}$–T relation is $L_{\rm X} \propto T^{3/2}E(z)$, and our best-fitting slope $B_{\rm lt} = 2.28^{+0.28}_{-0.26}$ is in 3σ tension with the self-similar prediction. Since advanced X-ray instruments enabled measuring luminosity and temperature of clusters large enough to form statistical samples, a similar tension has been reported in many independent studies (e.g., Pratt et al. 2009; Eckmiller et al. 2011; Maughan et al. 2012; Hilton et al. 2012; Lovisari et al. 2015; Zou et al. 2016; Giles et al. 2016; Bahar et al. 2022). Tension with the self-similar model is expected to emerge if one or more assumptions of the Kaiser (1986) model are violated. The usual suspect for this violation is the self-similar model not including nongravitational feedback mechanisms such as AGN feedback. Both $L_{\rm X}$ and T are vulnerable to such baryonic processes, and therefore the change in slope of the $L_{\rm X}$–T relation compared to the self-similar prediction is governed by the complex relationship between the nongravitational mechanisms and their effects on these observables.

Furthermore, the best-fit value of the slope we found in this work ($B_{\rm lt} = 2.28^{+0.28}_{-0.26}$) is broadly consistent but slightly

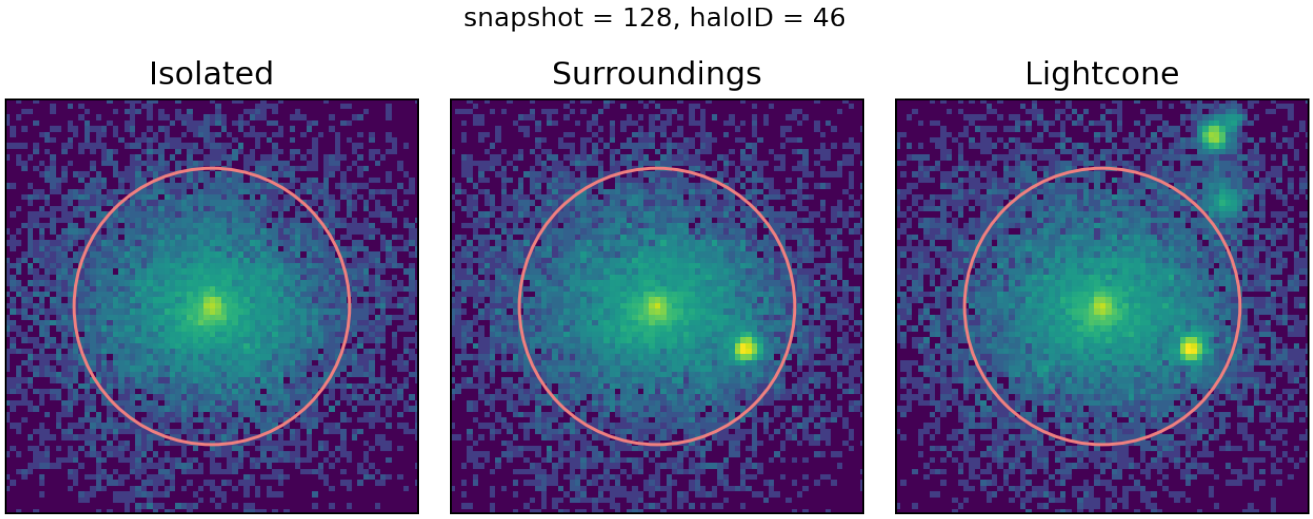

Fig. 12. Mock eROSITA image of the cluster in snapshot 128 with halo ID 46. It has the lowest $(kT_{\rm surr} - kT_{\rm iso})/kT_{\rm iso}$ and the highest $(L_{\rm surr} - L_{\rm iso})/L_{\rm iso}$. All events are shown, and no background is included in the image. The circle indicates a radius of $r_{\rm 500c}$.

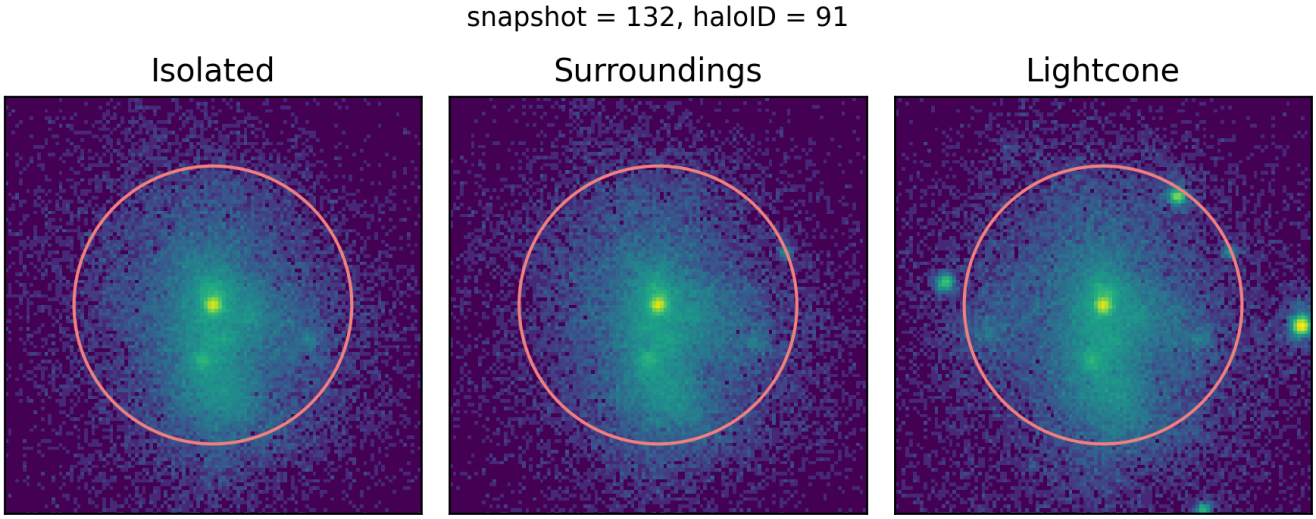

Fig. 13. Mock eROSITA image of the cluster in snapshot 132 with halo ID 91. It has the lowest $(kT_{\rm lc} - kT_{\rm surr})/kT_{\rm surr}$. All events are shown, and no background is included in the image. The circle indicates a radius of $r_{\rm 500c}$.

shallower than the most recent studies in the literature where the selection effects are taken into account in a sophisticated manner (Lovisari et al. 2015; Giles et al. 2016; Bahar et al. 2022). Our results for the slope lies within 2σ statistical uncertainty with the results presented in Bahar et al. (2022; $B_{\rm lt} = 2.89^{+0.14}_{-0.13}$) and within 1.3σ statistical uncertainty with the results presented in Giles et al. (2016; $B_{\rm lt} = 2.63 \pm 0.15$) and Lovisari et al. (2015; $B_{\rm lt} = 2.67 \pm 0.11$). We argue that the origin of the slope mismatch may be due to two reasons. The first possible cause is that investigating the $L_{\rm X}$–T relation using samples living in different mass parameter spaces may be leading to slightly different results. The cluster sample used in this work is obtained by applying a mass cut of $>10^{14}\,M_{\odot}$, which results in the sample being made up of mostly $M_{\rm 500c} \sim 10^{14}\,M_{\odot}$ clusters because of the steep mass function. However, for example, the sample used in Bahar et al. (2022) contains a significant amount of galaxy groups that cover $<10^{14}\,M_{\odot}$ parameter space. Lovisari et al. (2015) found galaxy groups having a steeper $L_{\rm X}$–T relation when they compared their results obtained for their galaxy groups sample ($B_{\rm lt} = 2.86 \pm 0.29$) and their high-mass sample ($B_{\rm lt} = 2.55 \pm 0.27$). The second possible reason for the slight mismatch is that the implementation of nongravitational processes in simulations is challenging, and differences in the chosen models for these can alter these relations. Recently there has been a significant improvement in implementing nongravitational feedback mechanisms in simulations; however, it is an open question whether the modeling is accurate enough to study the relation $L_{\rm X}$–T, which is arguably affected the most by these mechanisms.

In addition to having broadly consistent findings with the recently reported results that fully take into account the selection effects, our best-fitting slope is also consistent with other results in the literature. The slope reported in Kettula et al. (2015; $B_{\rm lt} = 2.52 \pm 0.10$) and Eckmiller et al. (2011; $B_{\rm lt} = 2.52 \pm 0.17$) are also slightly steeper but in very good agreement with our results. Pratt et al. (2009) reported a slope of $B_{\rm lt} = 2.24 \pm 0.25$, which is very close to our results, whereas the error bar of their measurement is relatively large. Biffi et al. (2013) found a slope of $B_{\rm lt} = 1.97 \pm 0.23$ for a smaller set of clusters from a lower-resolution version of the Magneticum simulation used in this work. Biffi et al. (2014) studied the same relation

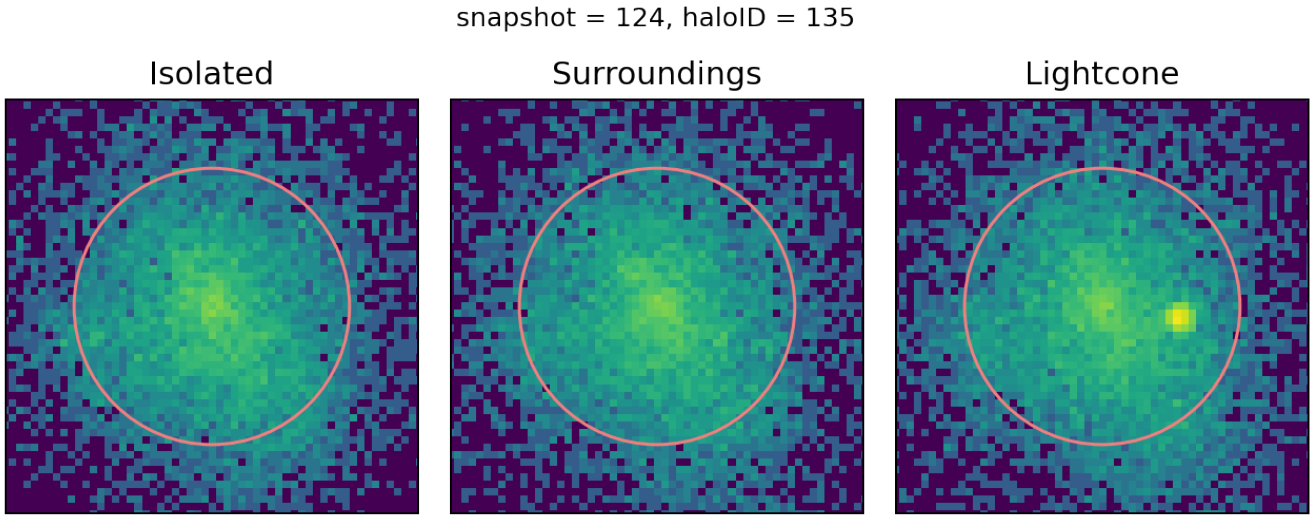

Fig. 14. Mock eROSITA image of the cluster in snapshot 124 with halo ID 135. It has the highest $(L_{\rm lc} - L_{\rm surr})/L_{\rm surr}$. All events are shown, and no background is included in the image. The circle indicates a radius of $r_{\rm 500c}$.

Table 4. Median values of observables measured for the three samples.

Parameters	Median/pivots
$L_{\rm X,lightcone}$	4×10^{43} erg s^{-1}
$L_{\rm X,slice}$	3.95×10^{43} erg s^{-1}
$L_{\rm X,isolated}$	3.99×10^{43} erg s^{-1}
$T_{\rm lightcone}$	2.26 keV
$T_{\rm slice}$	2.29 keV
$T_{\rm isolated}$	2.29 keV
$M_{\rm 500c}$	$3 \times 10^{14}\ M_\odot$
z	0.15

Notes. The values listed here are used as pivot values of observables in Eq. (6).

Table 5. Priors used for fitting the $L_{\rm X}$–T relations.

Free parameter	Prior
$A_{\rm lt}$	$\mathcal{U}(-4, 4)$
$B_{\rm lt}$	$\mathcal{U}(-10, 10)$
$C_{\rm lt}$	$\mathcal{U}(-10, 10)$
$A_{\rm tm}$	$\mathcal{N}(1.45, 0.14)$
$B_{\rm tm}$	$\mathcal{N}(0.65, 0.11)$
$C_{\rm tm}$	$\mathcal{N}(0.66, 1)$
$\sigma_{L_{\rm X}\|T}$	$\mathcal{U}(10^{-4}, 10)$
ρ	$\mathcal{U}(-10^{-3}, 10^{-3})$
$\sigma_{T\|M_{\rm 500c}}$	$\mathcal{N}(0.2, 0.023)$

using Marenostrum MUltidark SImulations of galaxy Clusters (MUSIC) data set and found a slope of $B_{\rm lt} = 2.24 \pm 0.25$ when they used the BCES bisector (Y, X) method, which is also in good agreement with our findings. Our cluster sample covers a redshift range of 0.03–0.17, which is relatively small compared to the redshift span of other samples used in observational studies. This results in our best-fit redshift evolution parameter being unconstrained $C_{\rm lt} = 1.47^{+2.32}_{-2.38}$. We note that even if the redshift evolution parameter cannot be constrained, it is better to have it as a free parameter in order to have the most realistic statistical uncertainties possible on other parameters. For intrinsic scatter of the $L_{\rm X}$–T relation, we found a best-fit value of $\sigma_{L_{\rm X}|T} = 0.27^{+0.06}_{-0.05}$. Our finding is considerably smaller than the previously reported results by Bahar et al. (2022; $\sigma_{L_{\rm X}|T} = 0.78^{+0.08}_{-0.07}$) and Pratt et al. (2009; $\sigma_{L_{\rm X}|T} = 0.76 \pm 0.14$), whereas still smaller but $\sim 2\sigma$ away from the scatter reported in Giles et al. (2016; $\sigma_{L_{\rm X}|T} = 0.47 \pm 0.07$). Finding a smaller intrinsic scatter could be due to insufficient modeling at various steps in both observational measurements and simulations. On the observation side, any observational or physical fluctuation that is not modeled, other than the physical intrinsic scatter of clusters, will add to the intrinsic scatter, and on the simulation side, any observational or physical fluctuation that is missing or underestimated in the photon simulations will result in low scatter. Linking the scatter in simulations and observations exceeds the scope of this work, and therefore we leave the investigation to future work.

We note that there are no mass measurements included in our Bayesian fitting framework. The T–$M_{\rm 500c}$ relation and the mass integral are included only to robustly model the mass-dependent cluster selection. Therefore, constraining the T–$M_{\rm 500c}$ relation is not among the primary goals of this work. The sampling distribution of the parameters $A_{\rm tm}$, $B_{\rm tm}$, and $C_{\rm tm}$ are mostly driven by their priors. The scattered T–$M_{\rm 500c}$ relation modeled in this work only has an impact on the modeled $L_{\rm X}$–T distribution through the lowest $\hat{L}_{\rm X}$, $\hat{T}$ measurements where the mass-dependent selection has the most prominent effect on the likelihood along the $L_{\rm X}$–T plane. As a result, and not surprisingly, the best-fit values of the $A_{\rm tm}$, $B_{\rm tm}$, and $C_{\rm tm}$ parameters for all samples are within the 2σ confidence region of the prior distribution. Lastly, we reran our fitting pipeline with uniform priors on the scaling relation parameters of the T–$M_{\rm 500c}$ relation in order to investigate the impact of the priors on the best-fit parameters of the $L_{\rm X}$–T relation. We find the results for the $L_{\rm X}$–T relations are all well within 1σ statistical uncertainty of the results with Gaussian priors, whereas, as expected, the chains for the T–$M_{\rm 500c}$ relation parameters wander around in unrealistic parameter space due to the lack of T and $M_{\rm 500c}$ measurements.

4. Conclusions

In this work we carried out an analysis of mock eROSITA observations of 84 clusters from the Magneticum `Box2_hr`

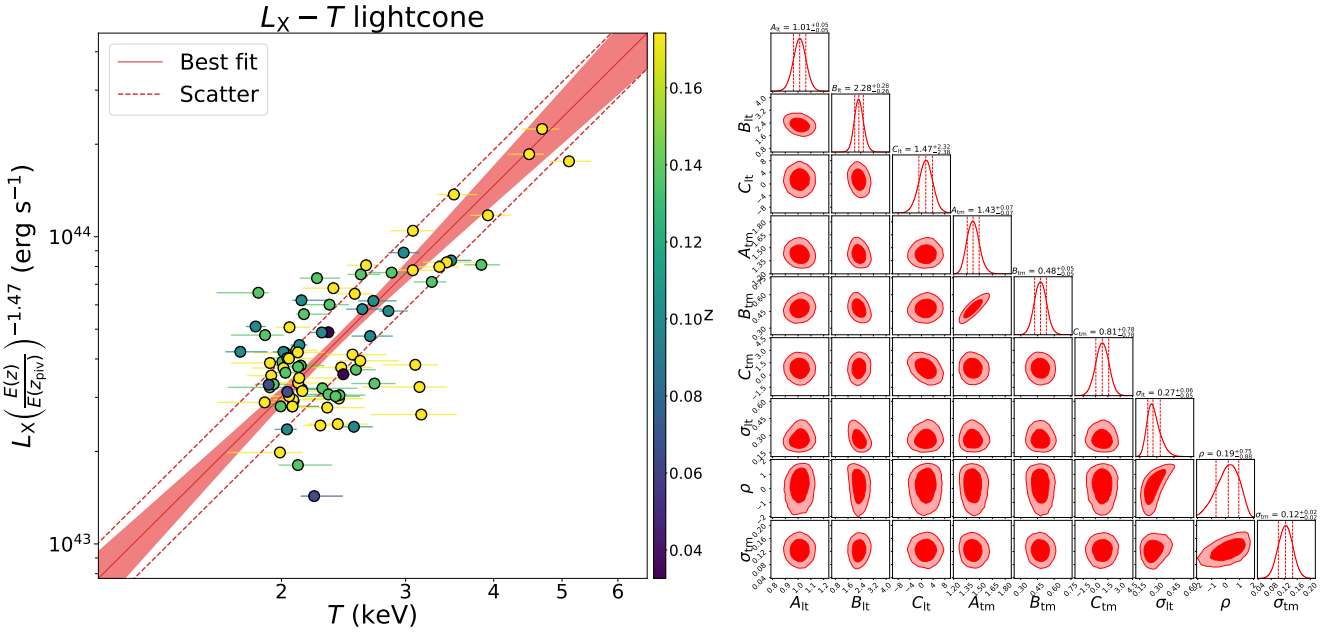

Fig. 15. Results of the L_X–T scaling relation analysis. *Left*: best-fitting scaling relation model to the soft band (0.5–2.0 keV) X-ray luminosity (L_X), temperature (T), and redshift (z) measurements of the lightcone sample. The solid red line represents the best-fit line, the red shaded area represents $\pm1\sigma$ uncertainty of the mean of the relation (see first row of μ in Eq. (6)), and the dashed red line represents the intrinsic scatter of the relation ($\sigma_{L|T}$) around the mean. *Right*: marginal and joint posterior distributions of the jointly modeled L_X–T and T–M_{500c} relations obtained from the second half of the MCMC chains. The red dashed vertical lines indicate the 32nd, 50th, and 68th percentiles, and the contours indicate the 68% and 95% credibility regions.

Table 6. Best-fit parameters of the L_X–T and T–M_{500c} relations for different samples.

Sample	A_{lt}	B_{lt}	C_{lt}	A_{tm}	B_{tm}	C_{tm}	$\sigma_{L_X\|T}$	ρ	$\sigma_{T\|M_{500c}}$
Lightcone	$1.01^{+0.05}_{-0.05}$	$2.28^{+0.28}_{-0.26}$	$1.47^{+2.32}_{-2.38}$	$1.43^{+0.07}_{-0.07}$	$0.48^{+0.05}_{-0.05}$	$0.81^{+0.78}_{-0.78}$	$0.27^{+0.06}_{-0.05}$	$0.19^{+0.75}_{-0.88}$	$0.12^{+0.02}_{-0.02}$
Surroundings	$1.03^{+0.05}_{-0.05}$	$2.26^{+0.29}_{-0.26}$	$1.18^{+2.34}_{-2.54}$	$1.41^{+0.07}_{-0.06}$	$0.48^{+0.05}_{-0.05}$	$0.87^{+0.78}_{-0.79}$	$0.28^{+0.06}_{-0.05}$	$0.24^{+0.71}_{-0.84}$	$0.13^{+0.02}_{-0.02}$
Isolated	$1.02^{+0.05}_{-0.05}$	$2.29^{+0.29}_{-0.27}$	$1.40^{+2.46}_{-2.50}$	$1.42^{+0.07}_{-0.06}$	$0.48^{+0.06}_{-0.05}$	$0.78^{+0.80}_{-0.79}$	$0.27^{+0.06}_{-0.05}$	$0.20^{+0.72}_{-0.88}$	$0.13^{+0.02}_{-0.02}$

Notes. Fitted relations are of the forms $L_X = A_{lt}\ L_{X,piv}\left(\frac{T}{T_{piv}}\right)^{B_{lt}}\left(\frac{E(z)}{E(z_{piv})}\right)^{C_{lt}}$ and $T = A_{tm}\ T_{piv}\left(\frac{M_{500c}}{M_{500c,piv}}\right)^{B_{tm}}\left(\frac{E(z)}{E(z_{piv})}\right)^{C_{tm}}$ with log-normal intrinsic scatters $\sigma_{L_X|T}$ and $\sigma_{T|M_{500c}}$ (in natural log). The pivot values used in these relations are provided in Table 4. These relations are connected to each other via the common observable T and a cross-correlation parameter ρ. Detailed description of the joint modeling and fitting of these relations as a multivariate normal distribution in log-log-log L_X–T–M space can be found in Sect. 3.5. The errors provided here were obtained from the second half of the MCMC chains and represent 1σ statistical uncertainties.

cosmological simulation, which were processed through the SIXTE simulator. Our conclusions are as follows:

– We first produced simple simulations of thermal spectra with lognormal temperature distributions convolved with the eROSITA responses, over a range of central temperatures $\ln kT_0$ and spreads $\ln\sigma$. We found that for values of $\ln\sigma \leq 0.2$, the temperature obtained from single-temperature fits is always $\lesssim$5% from the central temperature, but for larger values of $\ln\sigma$ the fitted temperature more significantly underestimates the central temperature by ∼20–30% at $kT \sim 1$–2 keV (depending on the redshift and metallicity) and up to ∼50% at higher temperatures ($kT \gtrsim 10$ keV) and much lower temperatures ($kT \lesssim 0.6$ keV). However, these extreme temperatures will not be the focus of cluster studies with eROSITA.

– We derived a spectroscopic-like temperature for the clusters in our sample along the lines of Mazzotta et al. (2004), and determined that a weighting function of $w = n_e n_p T^{-\alpha}$ with $\alpha = 0.76^{+0.05}_{-0.04}$ (assuming a cylindrical region of r_{500c} for computing the weights of the gas particles in the clusters) is the best fit to our sample, which is consistent with the value from M04. If we compute the weights using all of the gas particles within the spherical region r_{500c}, the best-fit $\alpha = 0.85^{+0.05}_{-0.03}$. The 1σ accuracy of this temperature compared with the fitted temperature is ∼8%, with some differences of as much as ∼20%, which is not nearly as accurate as the T_{sl} derived for clusters with $kT \gtrsim 2$–3 keV and *Chandra* and *XMM-Newton* observations by M04. Investigating a way to more accurately predict of single-temperature fits to eROSITA spectra from simulations is left for future work. We also compared the fractional difference of the fitted temperature to the log-normal central temperature from the SPH particles to the same quantity from the toy models, and find general agreement.

– We also compared the luminosities computed directly from the simulation gas particles to the luminosities estimated

from single-temperature fits, both within an overdensity radius of r_{500c}. If spheres of r_{500c} are used, the fitted luminosity overestimates the actual luminosity by ∼6% on average since the former uses emission projected within a cylindrical region along the line of sight within the same radius. If we instead make a comparison to the simulation-derived luminosity within the same cylindrical region, the agreement is improved, though there is still a scatter of ∼5% between the simulation and fitted estimates. This scatter originates from fitting single-temperature and metallicity models to spectra that include emission from gas at various temperatures and metallicities.

– We compared temperatures and luminosities from three different samples for the 84 clusters, where other structures in projection were progressively added, first near each cluster at roughly the same redshift, and finally across a lightcone of emission over a range of redshift. We find that the differences in temperature and luminosity between these samples are all very small, with mean differences on the order of ∼1−2% and 1σ scatter of ∼2−3%. The most extreme examples of differences in luminosity and temperature arise from obvious projections of structures external to the main cluster under consideration that may be easily accounted for in analysis.
– We fitted an L_X−T relation to the eROSITA-like measurements for the three different samples following a Bayesian approach by jointly modeling L_X−T and T−M_{500c} relations in order to take into account the selection effects and the mass function. We constrained the L_X−T relation through mock observed $\hat{L}_X$ and $\hat{T}$ measurements and T−M_{500c} scaling relation parameters are left free with priors taken from the literature in order to robustly model the selection function. Parallel to the similarities in L_X and T measurements, we find the best-fit parameters of the L_X−T relation of different samples are practically the same within the error bars. Furthermore, we compared our L_X−T scaling relation results with the literature for the lightcone sample, which is closest to the eROSITA observations. We found our slope ($B_{lt} = 2.28^{+0.28}_{-0.26}$) to be broadly consistent but slightly shallower than the recently reported results that fully account for the selection effects. Given the limited redshift span of our cluster sample, our fitting machinery was unable to constrain the redshift evolution ($C_{lt} = 1.47^{+2.32}_{-2.38}$); however, its contribution to the uncertainties of other measurements is included. Compared to the literature, we found a smaller intrinsic scatter ($\sigma_{L_X|T} = 0.27^{+0.06}_{-0.05}$), which we argue may indicate insufficient modeling of observational and/or physical variations in observational studies and/or in simulations.

Overall, the bias in temperature and luminosity of clusters induced by projection effects from structures outside the system in question is very small for almost all of the clusters in our sample. This bias is smaller than the expected statistical errors from the eROSITA observations, systematic differences due to fitting single-temperature models to multi-temperature gas, and the bias induced by using a projected luminosity to estimate a luminosity value computed within a sphere of the same radius. This indicates that consideration of projection effects from external structures should not be a large concern for studies using observed properties of clusters as mass proxies for constraining cosmological parameters, and the focus should be on differences arising from multiphase gas and geometrical considerations.

These conclusions necessarily come with some caveats. Our analysis should be extended to larger sample sizes of clusters, corresponding to lightcones with wider angular sizes. With larger sample sizes, chance alignments between clusters along the line of sight will inevitably increase. When studying larger samples, it would also be instructive to examine the effect of varying cosmological parameters on projection effects, especially those parameters which would increase the number of chance alignments between clusters (though for the range of cosmological parameters currently permitted by observations these effects are likely to be small). The most significant projection effects would occur in systems for which our line of sight is aligned by chance with a cosmic filament stretching megaparsecs in length at the same location as the target cluster on the sky. Constructing mocks from cosmological simulations where such alignments are purposefully chosen could give a worst-case estimate of projection effects. Finally, in this paper we used all of the simulated counts from each cluster in the analysis. Given the variation in core properties in clusters, many analyses of scaling relations work instead with core-excised quantities. It would be interesting to perform this same analysis with core-excised quantities, and also investigate the properties of clusters in merging versus relaxed samples. We leave these considerations for future work.

Acknowledgements. The Magneticum Pathfinder simulations have been performed at the Leibniz-Rechenzentrum with CPU time assigned to the projects pr86re and pr83li. J.A.Z. thanks Alexey Vikhlinin and Urmila Chadayammuri for useful discussions. J.A.Z. acknowledges support from the *Chandra* X-ray Center, which is operated by the Smithsonian Astrophysical Observatory for and on behalf of NASA under contract NAS8-03060. E.B. acknowledges financial support from the European Research Council (ERC) Consolidator Grant under the European Union's Horizon 2020 research and innovation programme (grant agreement CoG DarkQuest No. 101002585). V.B. acknowledges support by the Deutsche Forschungsgemeinschaft (DFG, German Research Foundation) – 415510302. K.D. acknowledges support by the COMPLEX project from the European Research Council (ERC) under the European Union's Horizon 2020 research and innovation program grant agreement ERC-2019-AdG 882679 and by the Excellence Cluster ORIGINS which is funded by the DFG under Germany's Excellence Strategy – EXC-2094 – 390783311. T.D. and O.K. acknowledge funding by the Deutsches Zentrum für Luft- und Raumfahrt contract 50 QR 2103. Software packages used in this work include: `PHOX` (`https://www.usm.uni-muenchen.de/~biffi/phox.html`) (Biffi et al. 2012, 2013); `SIXTE` (`https://www.sternwarte.uni-erlangen.de/sixte/`), (Dauser et al. 2019); AstroPy (`https://www.astropy.org`) (Astropy Collaboration 2013); Matplotlib; NumPy (`https://www.numpy.org`) (Harris et al. 2020); yt (`https://yt-project.org`), (Turk et al. 2011).

References

Astropy Collaboration (Robitaille, T. P., et al.) 2013, A&A, 558, A33
Bahar, Y. E., Bulbul, E., Clerc, N., et al. 2022, A&A, 661, A7
Becker, M. R., & Kravtsov, A. V. 2011, ApJ, 740, 25
Biffi, V., Dolag, K., Böhringer, H., & Lemson, G. 2012, MNRAS, 420, 3545
Biffi, V., Dolag, K., & Böhringer, H. 2013, MNRAS, 428, 1395
Biffi, V., Sembolini, F., De Petris, M., et al. 2014, MNRAS, 439, 588
Biffi, V., Dolag, K., Reiprich, T. H., et al. 2022, A&A, 661, A17
Brunner, H., Liu, T., Lamer, G., et al. 2022, A&A, 661, A1
Bulbul, G. E., Hasler, N., Bonamente, M., & Joy, M. 2010, ApJ, 720, 1038
Bulbul, E., Chiu, I. N., Mohr, J. J., et al. 2019, ApJ, 871, 50
Bulbul, E., Liu, A., Pasini, T., et al. 2022, A&A, 661, A10
Cash, W. 1979, ApJ, 228, 939
Chiu, I. N., Ghirardini, V., Liu, A., et al. 2022, A&A, 661, A11
Dauser, T., Falkner, S., Lorenz, M., et al. 2019, A&A, 630, A66
Davis, M., Efstathiou, G., Frenk, C. S., & White, S. D. M. 1985, ApJ, 292, 371
Dolag, K., Meneghetti, M., Moscardini, L., Rasia, E., & Bonaldi, A. 2006, MNRAS, 370, 656
Dolag, K., Borgani, S., Murante, G., & Springel, V. 2009, MNRAS, 399, 497
Dolag, K., Gaensler, B. M., Beck, A. M., & Beck, M. C. 2015, MNRAS, 451, 4277
Dolag, K., Mevius, E., & Remus, R.-S. 2017, Galaxies, 5, 35
Eckmiller, H. J., Hudson, D. S., & Reiprich, T. H. 2011, A&A, 535, A105
Ettori, S., Ghirardini, V., Eckert, D., et al. 2019, A&A, 621, A39
Ezer, C., Bulbul, E., Nihal Ercan, E., et al. 2017, ApJ, 836, 110
Foreman-Mackey, D., Hogg, D. W., Lang, D., & Goodman, J. 2013, PASP, 125, 306

Frank, K. A., Peterson, J. R., Andersson, K., Fabian, A. C., & Sanders, J. S. 2013, ApJ, 764, 46
Gianfagna, G., Rasia, E., Cui, W., et al. 2023, MNRAS, 518, 4238
Giles, P. A., Maughan, B. J., Pacaud, F., et al. 2016, A&A, 592, A3
Harris, C. R., Millman, K. J., van der Walt, S. J., et al. 2020, Nature, 585, 357
Hilton, M., Romer, A. K., Kay, S. T., et al. 2012, MNRAS, 424, 2086
Hirschmann, M., Dolag, K., Saro, A., et al. 2014, MNRAS, 442, 2304
Iljenkarevic, J., Reiprich, T. H., Pacaud, F., et al. 2022, A&A, 661, A26
Kaastra, J. S. 2017, A&A, 605, A51
Kaastra, J. S., Tamura, T., Peterson, J. R., et al. 2004, A&A, 413, 415
Kaiser, N. 1986, MNRAS, 222, 323
Kettula, K., Giodini, S., van Uitert, E., et al. 2015, MNRAS, 451, 1460
Komatsu, E., Smith, K. M., Dunkley, J., et al. 2011, ApJS, 192, 18
König, O., Wilms, J., Arcodia, R., et al. 2022, Nature, 605, 248
Lau, E. T., Nagai, D., Kravtsov, A. V., & Zentner, A. R. 2011, ApJ, 734, 93
Liu, A., Bulbul, E., Ghirardini, V., et al. 2022b, A&A, 661, A2
Liu, A., Bulbul, E., Ramos-Ceja, M. E., et al. 2023, A&A, 670, A96
Liu, T., Merloni, A., Comparat, J., et al. 2022a, A&A, 661, A27
Lovisari, L., Reiprich, T. H., & Schellenberger, G. 2015, A&A, 573, A118
Mantz, A. B. 2019, MNRAS, 485, 4863
Mantz, A. B., Allen, S. W., Morris, R. G., & von der Linden, A. 2018, MNRAS, 473, 3072
Maughan, B. J. 2007, ApJ, 668, 772
Maughan, B. J., Giles, P. A., Randall, S. W., Jones, C., & Forman, W. R. 2012, MNRAS, 421, 1583
Mazzotta, P., Rasia, E., Moscardini, L., & Tormen, G. 2004, MNRAS, 354, 10
McCammon, D., Almy, R., Apodaca, E., et al. 2002, ApJ, 576, 188
Mernier, F., & Biffi, V. 2022, in Handbook of X-ray and Gamma-ray Astrophysics, eds. C. Bambi & A. Santangelo, (Springer, Singapore)
Morrison, R., & McCammon, D. 1983, ApJ, 270, 119
Pacaud, F., Clerc, N., Giles, P. A., et al. 2016, A&A, 592, A2
Peterson, J. R., Kahn, S. M., Paerels, F. B. S., et al. 2003, ApJ, 590, 207
Pratt, G. W., Croston, J. H., Arnaud, M., & Böhringer, H. 2009, A&A, 498, 361
Pratt, G. W., Arnaud, M., Biviano, A., et al. 2019, Space Sci. Rev., 215, 25
Predehl, P., Andritschke, R., Arefiev, V., et al. 2021, A&A, 647, A1
Puchwein, E., Sijacki, D., & Springel, V. 2008, ApJ, 687, L53
Ramos-Ceja, M. E., Oguri, M., Miyazaki, S., et al. 2022, A&A, 661, A14
Sanders, J. S., Biffi, V., Brüggen, M., et al. 2022, A&A, 661, A36
Scheck, D., Sanders, J. S., Biffi, V., et al. 2023, A&A, 670, A33
Schellenberger, G., Reiprich, T. H., Lovisari, L., Nevalainen, J., & David, L. 2015, A&A, 575, A30
Smith, R. K., Brickhouse, N. S., Liedahl, D. A., & Raymond, J. C. 2001, ApJ, 556, L91
Springel, V. 2005, MNRAS, 364, 1105
Springel, V., White, S. D. M., Tormen, G., & Kauffmann, G. 2001, MNRAS, 328, 726
Sunyaev, R., Arefiev, V., Babyshkin, V., et al. 2021, A&A, 656, A132
Tinker, J., Kravtsov, A. V., Klypin, A., et al. 2008, ApJ, 688, 709
Turk, M. J., Smith, B. D., Oishi, J. S., et al. 2011, ApJ, 192, 9
Veronica, A., Su, Y., Biffi, V., et al. 2022, A&A, 661, A46
Vikhlinin, A. 2006, ApJ, 640, 710
Whelan, B., Veronica, A., Pacaud, F., et al. 2022, A&A, 663, A171
Zou, S., Maughan, B. J., Giles, P. A., et al. 2016, MNRAS, 463, 820

Appendix A: Fitting with and without background

All of the temperatures and luminosities of the clusters reported in Section 3 were obtained from spectral fits with background components included in the data and model. In this section we report the fitted temperatures and luminosities of the isolated cluster sample without background and compare them to those with background. The fits without background are otherwise identical to those with background; for example, the same energy range is used in the fit and the same source parameters are frozen and thawed.

Figure A.1 shows the fitted temperatures of the isolated cluster sample with and without background plotted against each other in the left panel, and with their difference plotted against the fitted temperature without background in the right panel. The fitted temperatures with background are typically biased low compared to those without, but the difference is well within the 1σ errors. Lower-temperature clusters are primarily affected by the astrophysical background and foreground, whereas higher-temperature clusters can also be affected by the non-X-ray background.

Figure A.2 shows the fitted luminosities of the isolated cluster sample with and without background plotted against each other in the left panel, and with their difference plotted against the fitted luminosities without background in the right panel. The fitted luminosities with background are all biased low compared to those without, but the difference is very small and almost always within the 1σ error.

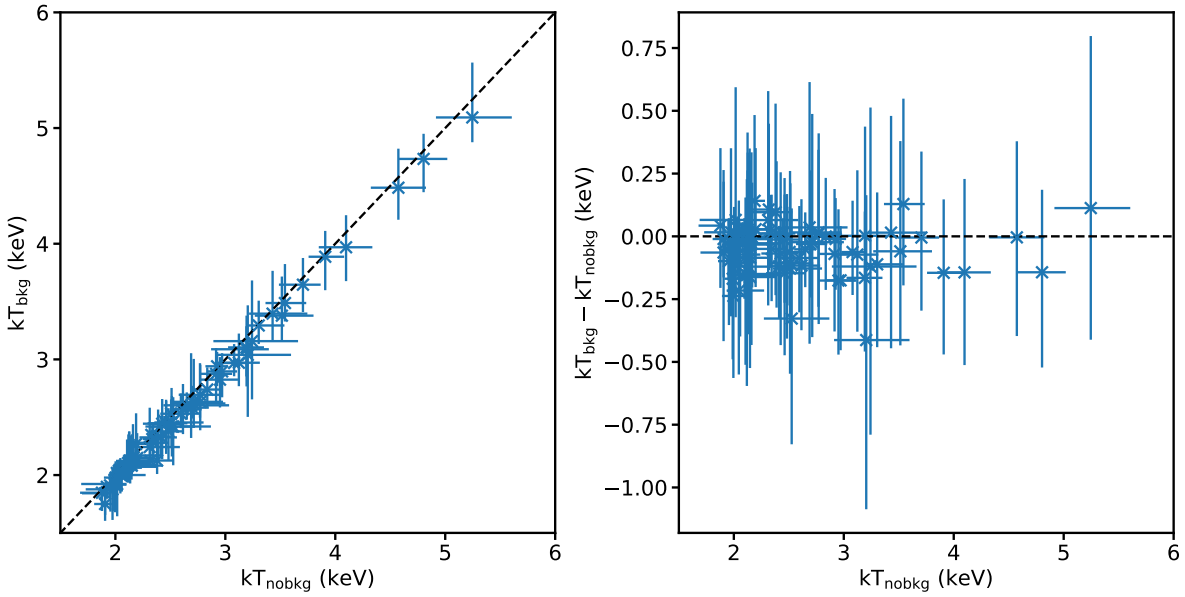

Fig. A.1. Fitted temperatures of the isolated cluster sample with and without background. Left panel: Temperature with background vs. temperature without background. The black dashed line indicates equality between the two temperatures. Right panel: Difference between the two temperatures vs. the temperature without background. The black dashed line indicates no difference between the temperatures.

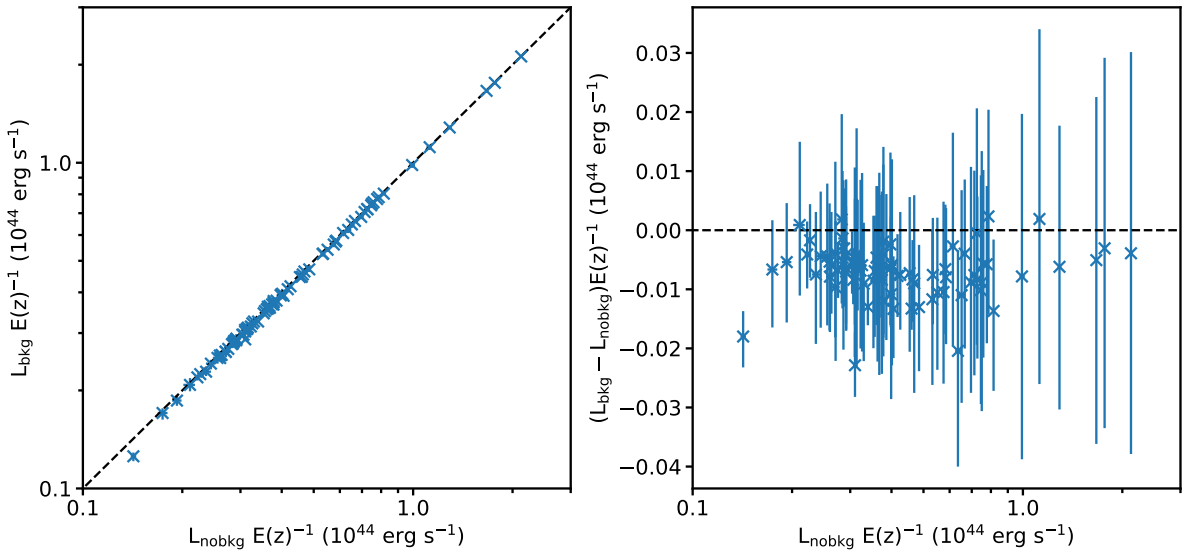

Fig. A.2. Fitted luminosities of the isolated cluster sample with and without background. Left panel: Luminosity with background vs. luminosity without background. The black dashed line indicates equality between the two luminosities. Right panel: Difference between the two luminosities vs. the luminosity without background. The black dashed line indicates no difference between the luminosities.